



Impact of Second Phase Content on Rock Salt Rheological Behavior Under Cyclic Mechanical Conditions

Carla Martin-Clave¹ · Audrey Ougier-Simonin² · Veerle Vandeginste^{1,2}

Received: 29 July 2020 / Accepted: 18 March 2021 / Published online: 5 April 2021
© The Author(s) 2021

Abstract

Safe Underground Gas Storage (UGS) can be achieved in artificial, salt caverns to meet fluctuations in energy demand by providing adequate knowledge on rock salt when subjected to similar cyclic conditions. In this study, we performed cyclic mechanical tests on five rock salt samples with different types and amounts of second-phase mineral content. A confining pressure of 25 MPa was applied, whilst the axial stress was cycled between 4.5 and 7.5 MPa, at 0.5 kN/s loading rate, during 48 h (7200 cycles). The results demonstrate that high second-phase content such as anhydrite layering operates as a strength weakening agent by accommodating larger brittle deformation in comparison to samples with a lower content in secondary minerals. This rheological behavior is further exacerbated by the cycling mechanical conditions and recorded by a marked step on Young's modulus and Poisson's ratio value evolution. The microstructure analysis reveals how halite grains accommodate most of the deformation induced by the cyclic mechanical loading conditions through brittle deformation with microfracturing network development. Other structures from different deformation mechanisms are also discussed. Two types of new porosity are observed: (i) pores around isolated crystals of second-phase minerals as a result of grain rotation under cyclic mechanical deformation, and (ii) microcracks in areas with high concentration of secondary minerals (such as anhydrite, polyhalite, carnallite, or kieserite). This porosity change has strong implications for both the mechanical behavior of the material and its potential permeability.

Keywords Halite · Cyclic mechanical loading · Elastic parameters · Porosity · Underground gas storage

1 Introduction

The use of caverns in rock salt (halite) for Underground Gas Storage (UGS) and Compressed Air Energy Storage (CAES) has been identified as a strategic option to meet seasonal energy demand fluctuations in the electricity grid (Ozarlan 2012; Evans and Chadwick 2009; British Geological Survey 2016; Peach 1991). UGS, used to meet the seasonal fluctuations in energy demand, operates with moderate gas production rate and just one or few cycles per year. UGS has been also assessed as a more feasible option for short-term peak shaving operations compared to surface gas tanks. Indeed, salt caverns present lower specific construction costs,

smaller surface footprint, and very high level of protection from external influences. The combination of big volumes and large range of operating pressures allows a typical large salt cavern to hold more than 60 times the volume of traditional gas tank (Michalski et al. 2017). CAES is a promising solution for energy storage with a significant and growing scientific and economic interest to support intermittent sources of renewable energy such as wind energy (Bérest Pierre et al. 2013; Bullough Chris et al. 2004; Lund and Salgi 2009). It also implies that CAES present daily cycles of injection-withdrawal operations compared to UGS (Bérest Pierre et al. 2013).

Salt caverns have also been identified as a key element in the UK energy system decarbonization strategy for storing hydrogen (Sadler 2016), for power generation purposes to meet the UK government target to reduce greenhouse emissions (Parliament 2008). Hydrogen is presented as the only gas decarbonization option suitable to replace natural gas, by doing some modifications to the current gas networks,

✉ Carla Martin-Clave
Carla.MartinClave@nottingham.ac.uk

¹ School of Chemistry, Vaughan Parry Williams Pavilion, Clifton Blvd, Nottingham NG7 2RD, UK

² British Geological Survey, Nicker Hill, Keyworth, Nottingham NG12 5GG, UK

ensuring energy supply in the long term, from a cost-optimal perspective (Dodds and McDowall 2013).

Halite has low (i) creep strength, (ii) porosity, (iii) permeability, and iv) density, making it a very good seal rock (Bérest Pierre et al. 2012) capable of trapping hydrocarbons on a geological time scale for instance. The creation of caverns for UGS in halite formations and the operation activities of gas injection and withdrawal occurring under lithostatic pressure lead to local deviatoric stresses resulting in rock salt creep deformation (Carter et al. 1982; Van Sambeek et al. 1993). Additionally, periodic injection-production activities in response to seasonal temperature changes and associated gas consumption imply regular fluctuation of both mechanical (due to internal operational pressure changes) and thermal (due to adiabatic processes) stresses in salt caverns (Jiang et al. 2016; Fan et al. 2016). Therefore, understanding the fatigue of rock salt under these mechanical cyclic conditions is paramount to ensure safe and sustainable UGS (Fan et al. 2019).

Deformation in rock salt subjected to cyclic mechanical loading conditions is accommodated by dislocation motion and pressure solution, grain rupture, microcracks, and frictional sliding (Jiang et al. 2016; Fan et al. 2019). Other common deformation mechanisms are dislocation creep and solution-precipitation creep, which can imply different re-crystallization processes (Urai et al. 1986; Urai and Spiers 2007; Li and Urai 2016). Dislocation creep is promoted by lattice or crystal defects under stress and the main dynamic re-crystallization processes take place inside the crystal lattice of halite grains (Li and Urai 2016). Dynamic re-crystallization processes include grain boundary sliding (GBS), trans-granular microcracking and dislocation creep by grain boundary migration (GBM) and subgrain rotation (SR) (Urai et al. 1986; Urai and Spiers 2007; Urai 2008; Desbois et al. 2010; Závada 2015; Linckens et al. 2016). Pressure-solution creep (PS) or solution-precipitation creep takes place at the grain boundary enhanced by grain boundary brine. During pressure solution, grains dissolve at highly stressed boundaries and diffusion of the material through the grain boundaries results in re-crystallization at low normal stress interfaces (Urai and Spiers 2007). Rock salt deformation is generally a complex process involving more than one mechanism at once. As a result of the different re-crystallization processes, rock salt deforms as a viscous fluid under deviatoric stresses modifying the material strength and its lateral deformation capacity (Liang et al. 2011). In the long term, this can lead for example to a reduced cavern's volume (shrinking walls) down to cavern's closure (Brouard 2013). Our current knowledge on how this complex micromechanism relationship controls the overall stability and integrity of the caverns is incomplete.

Rock salt typically contains secondary mineral phases (e.g., anhydrite, polyhalite, carnallite, and kieserite), as well

as fluids trapped in inclusions in the halite crystals, at halite grain boundaries, or in pores. This presence of other minerals besides halite or other rock layers between the rock salt formations at a range of scales can have significant effects on the micro- and macro-mechanical properties due to their different rheological behaviors, notably weakening the rock salt under high stress conditions (Liang 2012; Berest et al. 2005, 2006; Ma et al. 2013; Serbin et al. 2015; Khaledi et al. 2016; Av et al. 2016; Li 2019). Second-phase content are known to contribute to a porosity increase (Li 2019) and can compromise the sealing integrity of rock salt. When subjected to mechanical loading, damage mainly develops in the form of microcracks along the interfaces between halite crystals and second mineral phase layers (Li 2019). An increase in second-phase content in halite can also lead to an increase in ductility as a result of a higher diffusion rate along the solid inclusion–halite contacts in comparison with halite–halite contacts (Závada 2015). The mechanical behavior and damage mechanisms of bedded rock salt depend on the interlayering material and, in particular, on the strength of the interface between different materials (Liang 2012). Yet, the effects of second-phase minerals content on halite rheological behavior under cyclic mechanical conditions are still not well understood.

Previous studies report on the behavior of halite under cyclic conditions and the rock salt cycle life, typically investigating the mechanical properties and rheological behavior of rock salt samples under cyclic conditions till complete sample failure (Fan et al. 2016; Liang 2012; Zhao 2020; Fan 2017; Zhenyu and Haihong 1990). Yet, monitoring the elastic parameter variations (such as Young's modulus, Poisson's ratio, and Bulk modulus) at the early stage of the deformation behavior in relation to the different rock salt compositions would bring essential information on halite mechanical stability with respect to gas storage risks (Xiong et al. 2015). Some authors show monitored acoustic emission from rock salt deformed under cyclic loading condition (Fan 2017; Voznesenskii et al. 2017) and dynamic Young's modulus from velocities of the longitudinal P- and transverse S-waves through sounding of the samples (Voznesenskii et al. 2017). This allows them to remotely observe the softening to hardening evolution of the halite when subjected to cyclic loading conditions.

In this study, we investigate the impact of the secondary mineral phase content on the rock salt mechanical behavior under cyclic loading conditions. Cyclic triaxial tests were performed on five rock salt samples with different types of secondary mineral phase content at 25 MPa confining pressure and ambient temperature (22°–25°C). Thin sections of each sample's microstructures, before and after mechanical deformation, were analysed by transmitted light microscopy and scanning electron microscopy (SEM) to identify the micromechanisms and early damage induced by the cyclic

loading conditions. Finally, we assess the role of the secondary mineral phase content on the microdamage development under cyclic stress changes to provide an insight on its potential impact in salt caverns during UGS activities.

2 Rock Salt Formations in the UK

The salt formations in the UK are of Triassic (252–201 Mya) and Permian age (299–251 Mya). Triassic salt in the UK can be found mainly in bedded strata in the Cheshire Basin and, to a lesser extent, in Northern Ireland, Lancashire, the Isle of Man and Walney, Staffordshire, Worcestershire, and Somerset. Permian salt fields extend in the northeast of England (Yorkshire) and Northern Ireland (Beutel and Black 2005). The rock salt samples tested are from Boulby Mine (Permian Zechstein) and Winsford Mine (Triassic Mercia Group) (Fig. 1).

2.1 Permian Rock Salt

Permian (299–251 Mya) salt deposits in the UK belong to the Zechstein Group sequence, which is found eastwards from the northeast of England in Yorkshire to Germany and

Poland. The Permian deposits from the Zechstein group crop out onshore only in the UK and are exploited in Boulby Mine. The Permian Zechstein sequence is composed mainly of thick units of anhydrite, halite, and potash. The Permian salt deposits in Yorkshire are divided in four cycles, which have been named Zechstein I–IV from the base upwards and originated as a cyclic drying out of a landlock sea in the Permian age (Beutel and Black 2005). Each cycle starts with a carbonate rock unit passing to anhydrite, polyhalite, and to halite. Other mineralogies associated with these Permian Zechstein rock salt deposits are kieserite, carnallite, and sylvinite. The thickest rock salt sequence in Yorkshire belongs to the second Zechstein cycle (Zechstein II) corresponding to Fordon Evaporites, with a thickness of 75–90 to 120 m. The Zechstein II has been assessed as a potential geological site to host salt caverns (Beutel and Black 2005).

Boulby Mine Boulby Mine is located in the Zechstein Permian Basin that extends from eastern England to the Netherlands, North Germany, and Poland (Ziegler 1990; Van Wees 2000; Zhang et al. 2013) (Fig. 1). The Zechstein salt sequence was deposited under arid climate conditions and as a result of a series of marine transgression and regression episodes during the Upper Permian (Zhang et al. 2013). The formation sequence presents clastic sediments of aeolian sandstones, fluvial fans, and shallow-lake deposits from Lower Permian passing through cyclic deposition of salt alternated with anhydrite and mudstone during the repeated transgression–regression episodes during the Upper Permian (Zhang et al. 2013; Strohmenger and Strauss 1996). Overlying the Upper Permian (Zechstein) formation of carbonates and evaporites, the sequence passes to red-bed fluvial to lacustrine sediments and sabkha deposits from the Lower Triassic and shallow marine carbonates from Middle Triassic (Zhang et al. 2013; Kossow and Krawczyk 2002). The deposition during the Mesozoic was controlled by the regression and transgression of the Tethys Ocean (Ziegler 1990; Zhang et al. 2013).

2.2 Triassic Rock Salt

Triassic (252–201 Mya) rock salt in the UK was deposited under semi-arid environmental conditions within mainly a fault-controlled endorheic basin linked to the major depositional centres of the North and Irish Sea (Cooper 2002) resulting in a brown–red and some slightly green–grey-colored sequences of evaporitic and sedimentary deposits (Cooper 2002; Howard et al. 2008). In the Cheshire Basin, the Mercia Mudstone Group consists of reddish-brown mudstones and siltstones alternating beds of halite (Evans and Holloway 2009). Within the Triassic Mercia Mudstone Group, the main rock salt resources are displayed in two salt-bearing formations, the lower Northwick Halite Formation with a maximum thickness of 280 m of pure halite beds

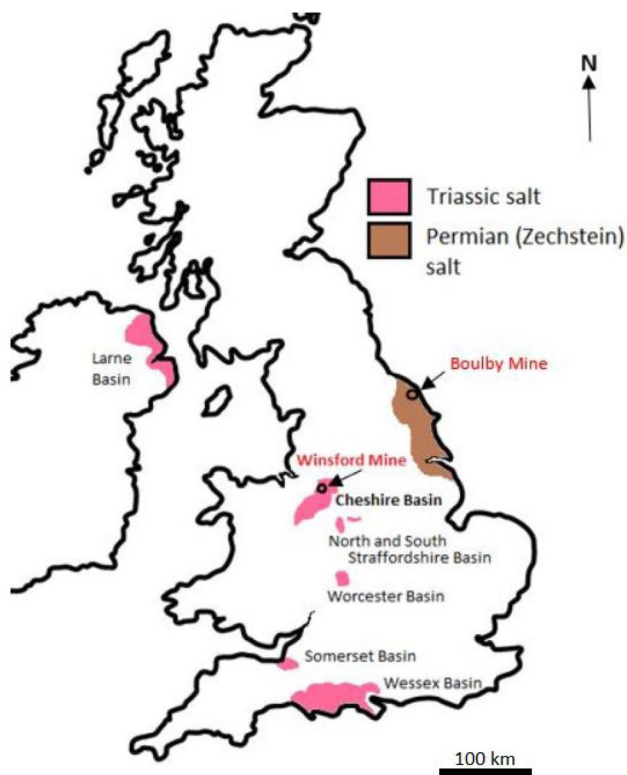


Fig. 1 Schematic map of the Triassic and Permian salt fields in the United Kingdom and Triassic basins. Winsford Mine is identified in the map as part of Cheshire Basin and Boulby Mine as part of the Zechstein Basin

alternating with mudstone and siltstone levels, and an upper Wilkesley Halite Formation in alternation with mudstone (Cooper 2002).

Winsford Mine

Winsford Mine is stratigraphically located at the base of the Northwich Halite Formation, which contains 92% NaCl, and the extraction is made by room and pillar mining (Norton et al. 2005). Within the salt mine, two different economically workable levels of rock salt have been differentiated on the halite purity, namely Zone B and Zone F. Zone B and Zone F are located between 130 and 200 m depth, respectively. Layer B has a higher concentration of halite, where the purest material is at the basal part of the salt bed. Layer F has a higher content of second phase mineralogy, mainly anhydrite and clay, and a lower concentration in halite. The geological formation, of approximately 150 m in thickness, was deposited during the Triassic under arid climatic conditions with terrigenous reddish-brown sediments containing red clay and other silicates. The mine extension and structure are limited by two main faults crossing the geological formation on the east and the west, and the mining activity in the site is limited to the zone in between the fault lines. During mining extension works in layer B, horizontal and vertical boreholes were drilled to delimit the location of the working horizon within the salt bed and the limits dictated by the structural settings of the site. The site engineers kindly provided core samples from the boreholes for testing in the laboratory. Additional rock salt samples were collected on site from layers B and F.

3 Methodology

3.1 Mineralogical Analysis

The mineralogical analysis was conducted by combining Powder X-Ray Diffraction (PXRD) analysis and polarized light microscopy using thin sections. Mineralogical phase identification by PXRD was completed on an X'Pert PRO PANalytical MPD X-ray diffractometer. Normal Bragg–Brentano geometry and CuK α radiation at 40 kV and 40 mA were used with sample holders of 20 mm diameter and samples were scanned over a sampling range of 5 to 70 2θ with a step size of 0.0066 ($^{\circ}2\theta$) and a scan speed of 0.23 2θ per second. For phase identification, the PDF4 (International Centre for Diffraction Data 2020) database was used within the software DIFFRAC.EVA to identify the mineral peak patterns. The PXRD data were combined with mineralogical description of blue dye impregnated, one-side polished thin sections at 200 microns. The thin section analysis was performed using a ZEISS transmitted light polarization microscope (using a magnification 10 \times and 20 \times).

3.2 Sample Preparation

Cylindrical samples of 51 mm diameter were cut from same diameter borehole cores using a diamond-tipped rock saw, so that the length-to-diameter ratio was approximately 2:1 (International Society for Rock Mechanics 1979). Off-cuts from each cylinder were used to produce thin sections previous to the cyclic mechanical loading test to provide information of the undamaged microstructure.

For the mechanical testing, each cylindrical sample was mounted between two hardened steel platens prepared with a layer of heat-resistant silicone tape for sealing purpose. The assembly was then encased in two 5 mm heat-shrink Polytetrafluoroethylene (PTFE) membranes to prevent ingress of confining fluid into the sample. Locking wires were used to complete the seal between the PTFE jacket and the platens. The sample was then instrumented with two axial extensometers (MTS 632.90F-12, accurate to $\pm 0.01\%$), positioned diametrically opposite each other over the central 50 mm of the sample, and a circumferential chain extensometer (MTS 632.92H-03, accurate to $\pm 0.01\%$) positioned at mid-length. A third platen, not part of the aforementioned sample assembly, was spherically seated to prevent eccentric loading. This spherically seated platen was in turn fixed to a 2.6 MN capacity force transducer (MTS 661.98B.01, accurate to $\pm 0.32\%$ of load) to measure the load applied to the sample.

After each test, the damaged sample was recovered, halved along the axial length (parallel to the applied axial stress), and impregnated in blue dye epoxy. A one-side polished thin section was then produced from the center of the sample, thicker (200 microns) than standard thin section due to the nature of halite minerals.

3.3 Cyclic Mechanical Loading Test

The cyclic mechanical loading tests were undertaken on a triaxial servo-controlled stiff frame (MTS 815 rock test system with a maximum axial load up to 4600 kN) with a confining pressure vessel rated to 140 MPa, at the Rock Mechanics and Physics Laboratory, British Geological Survey (BGS). A thermocouple was placed as close as possible to the sample to monitor the temperature. The confining pressure vessel was then closed and an initial axial load of $\sigma_1 = 1$ kN was applied, that corresponds to an axial stress of 0.5 MPa, to ensure a stable contact and alignment of the platens whilst the vessel was filled with mineral oil confining fluid. The confining pressure ($P_c = \sigma_2 = \sigma_3$) was then applied hydrostatically at 1 MPa/min to 25 MPa, and then kept constant at that value. The samples were all tested at room temperature between 22 $^{\circ}$ – 25 $^{\circ}$ and moisture conditions, in a single orientation.

The axial stress was cycled between 4.5 and 7.5 MPa at a loading rate of 0.5kN/s for a period of 48h. Hence, a

complete test comprised a total number of 7200 cycles. The axial load, axial load actuator displacement, axial stress (σ_1), differential stress ($Q = \sigma_1 - \sigma_3$), confining pressure P_c , confining pressure actuator displacement, axial strain (ϵ_{ax}), circumferential strain (ϵ_{circ}), and temperature were monitored throughout the test at two independent sampling frequencies of 5s and 2.5kN.

3.4 Microstructural Analysis

The microstructural analysis was performed on thin sections from Boulby mine samples only, before and after testing, using the same transmitted light microscope as for the mineralogical analysis, and a scanning electron microscope (SEM) to identify structures and deformation mechanisms resulting from the cyclic mechanical loading test. The same

thin sections used in the transmitted light microscope were treated with pulverized coated carbon to be used in the SEM.

4 Mineralogical Analysis and Sample Description

4.1 Mineralogical Analysis

The mineralogical results from the PXRD analysis are shown in Table 1. Each series result (A, B, C, F, LB) is an average of the compositional analysis performed on 5–12 core samples from that series. Samples from Boulby Mine were grouped in series A, B, and C, based on the petrological description (Fig. 2) and data from mineralogical analysis. Samples from Winsford Mine were grouped in series LB and F, based on the halite content level.

Table 1 Mineralogical characterisation from X-ray diffraction analysis; sd*= standard deviation

Mineral		A	B	C	F	LB
Halite	wt%	87	45	87	89	85
	sd*	7	22	3	12	8
Anhydrite	wt%	6	31	6	7	5
	sd	4	29	2	5	2
Illite	wt%	–	–	–	3	10
	sd	–	–	–	1	9
Quartz	wt%	–	–	–	0.6	0.3
	sd	–	–	–	0.12	0.04
Polyhalite	wt%	2	15	3	–	–
	sd	0.8	16	0.6	–	–
Kieserite	wt%	0.5	2	0.7	–	–
	sd	0.2	3	0.01	–	–
Carnallite	wt%	4	7	4	–	–
	sd	2	2	0.5	–	–

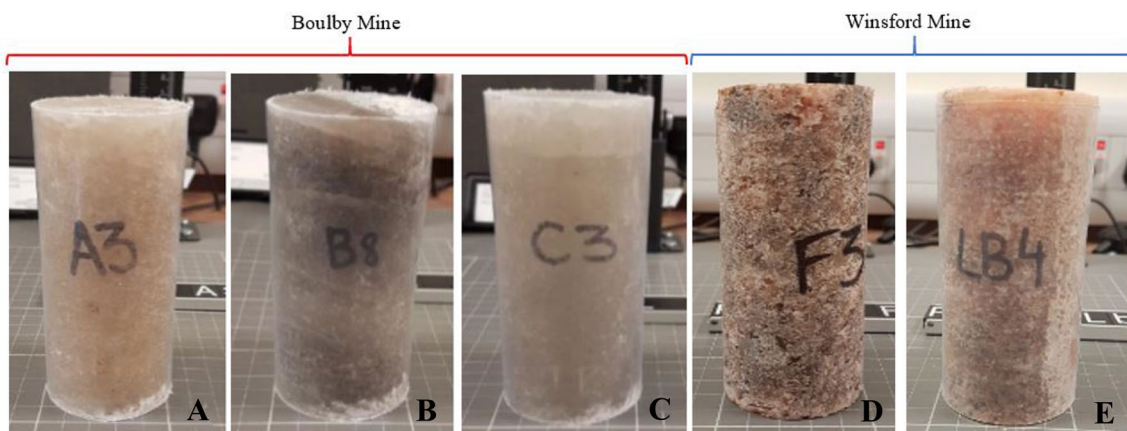


Fig. 2 Rock salt core samples used for the cyclic mechanical tests. From left to right, panels a–c correspond to Permian rock salt from Boulby Mine, and panels d and e correspond to Triassic rock salt samples from Winsford Mine

All series but series B had a very high content of halite of 86–90% on average. The highest amount of halite in average is measured in series A and C, with a halite content of around 86–87% and 87–88%, respectively. Series B has an average halite content of 45% and a strong layering related to significant variations in the second-phase content within the same core sample, with up to 30% anhydrite and 15% polyhalite. The percentage by weight has about 30% standard deviation due to the alternating halite and anhydrite thin layers. Series B also has a slightly higher content in carnallite (around 6–7%) and up to 5% kieserite was identified based on PXRD data.

4.2 Rock Salt Sample Description

Boulby Mine Permian rock salt samples were grouped in three different series; A, B, and C, according to the petrological description and second-phase content from the PXRD results combined with thin section analysis. Series A from *Boulby Mine* was described as clear halite, from white-transparent to light-brown color, with some thin layers (no more than 3 mm thick) of anhydrite sporadically in between halite layers at a 20° bedding dip angle (Fig. 2). However, series A core samples generally consist of clear rock salt crystals with average sizes of 1 mm to 1.5 cm. Thin section analysis indicates that the main mineralogy consists of halite and anhydrite (consistent with PXRD analysis). Two different ranges of grain size can be distinguished, (i) colorless or light-yellow halite crystals of 200 µm to 1.5 mm in diameter and which can contain fluid inclusions, and (ii) smaller prismatic anhydrite crystals with sizes of 10–200 µm in diameter. Both halite and anhydrite are colorless in plane polarized light, but under crossed polars, halite turns completely black due to the cubic crystal system, and anhydrite displays third-order interference colors from green and light blue to light pink (Fig. 3). Polyhalite occurs as colorless crystals with a maximum size of 200 µm, and displays low interference colors from grey to white and inclined extinction under crossed polarized light. This mineral also shows twinning typical of polyhalite (Biehl et al. 2014).

The distribution of second-phase content is mainly concentrated around the halite crystal boundaries, surrounding the anhedral and equant halite crystals (Fig. 3a, b). Occasionally, second-phase minerals are also included within some halite grains. Anhydrite tends to show spherical shapes, whereas polyhalite occurs as prismatic crystals. Kieserite is identified in the thin sections by a vitreous luster, very high birefringence and may have also twinning structures. Prismatic polyhalite can be observed poikilotopically enclosing finer crystals of anhydrite. Polyhalite crystals can be recognized under polarized light for the low interference colors and the chadacrysts of anhydrite enclosed in the oikocryst polyhalite are recognized by the third-order

interference colors. Polyhalite also shows parallel to inclined extinction.

Series B core samples show alternating 2 mm to 2 cm-thick layers of brown- and grey-colored anhydrite and very light grey to grey halite (Fig. 2b). Due to the insertion of halite and anhydritic rich layering, series B shows a higher variation in second-phase content (Table 1). Crystal size is slightly smaller than in series A and C, with grain sizes between microcrystalline and a few mm up to 1 cm. Based on thin section analysis, an increase in second-phase content such as anhydrite and polyhalite is noted. Thin sections reveal a significant increase in polyhalite, observed as prismatic shaped crystals, in comparison with the other core sample series (Fig. 3c, d). The anhydritic layering observed from the core sample (Fig. 2b) is seen as layers of microcrystalline anhydrite mud alternating with halite. The boundary between halite and anhydrite layers can be sharp or gradual. Figure 3e, f shows a well-defined discordant boundary of a microcrystalline matrix of anhydrite, abruptly cutting the halite crystals. On the top of the layer, a gradual mineralogical transition from anhydrite to halite can be observed. This transition presents a slight increase of anhydrite crystal size from the microcrystalline matrix to anhedral crystals from 10 to 50 µm and bigger halite crystals of 200 µm enclosing the smaller anhydrite crystals. In the anhydrite–halite contact zone, there are some fractures. The PXRD results indicate a halite content varying from 10 to 60% within the same sample. Second-phase content in Series B samples consist of anhydrite (6–30%), polyhalite (3–65%), kieserite (1–5%), and carnallite (5–10%) (Fig. 4).

Rock samples from series C do not show any layering. The sample shows clear white-greyish to light-grey salt crystals (Fig. 2c) with sizes from 1 mm to 1.5 cm. The PXRD analysis from series C identifies halite as the main mineralogy with the lowest variation in content in comparison to the other series tested. Series C also shows a small content of anhydrite (around 6%) and carnallite (around 4%) and very low content of polyhalite (3%) and kieserite (0.7%) (Table 1). The thin sections from series C show a structure formed by relatively bigger, in comparison with the previously discussed samples, halite crystals (from 500 µm to 1.5 cm) with lower second-phase content (Fig. 3g, h). Similar to the observations in the previous samples, the few second-phase minerals are generally located at the halite crystal boundaries, although small (about 10 µm) anhedral anhydrite crystals also occur enclosed in more central parts of the halite crystals.

Winsford Mine Samples from *Winsford Mine* are brown-to-reddish rock salt with crystal sizes of a few mm up to 2 cm (Fig. 2d, e). The PXRD (Table 1) and thin section petrographic results indicate that the main minerals are halite (84–90%) and anhydrite (1–13%), held in a reddish-colored clay matrix with some quartz crystals in very low quantities

Fig. 3 Microphotographs of Series A (a, b), Series B (c–f), and Series C (g, h) samples. **a** Large halite (Ha) crystals of up to 2 mm surrounded by small (about 50 μm) prismatic polyhalite crystals and small (about 20 μm) anhedral anhydrite (An) crystals. Sample A3, plane polarized light. **b** Same view as **a**, but under crossed polars. Halite crystals (black) are distinguished from polyhalite (indicated with the letter P) and anhydrite crystals (third-order interference colors). **c** Aggregate of prismatic polyhalite crystals and anhedral anhydrite grains enclosing halite crystals with maximum size of 200 μm . Plane polarized light. **d** Same view as **c**, but crossed polars. **e** Microcrystalline matrix of anhydrite layers alternating with halite. Plane polarized light. **f** Same view as **e**, but crossed polars. **g, h** Large (500 μm to 1 mm) halite crystals with small (up to 10 μm) anhedral anhydrite crystals located along the halite crystal grain boundaries. Plane polarized light

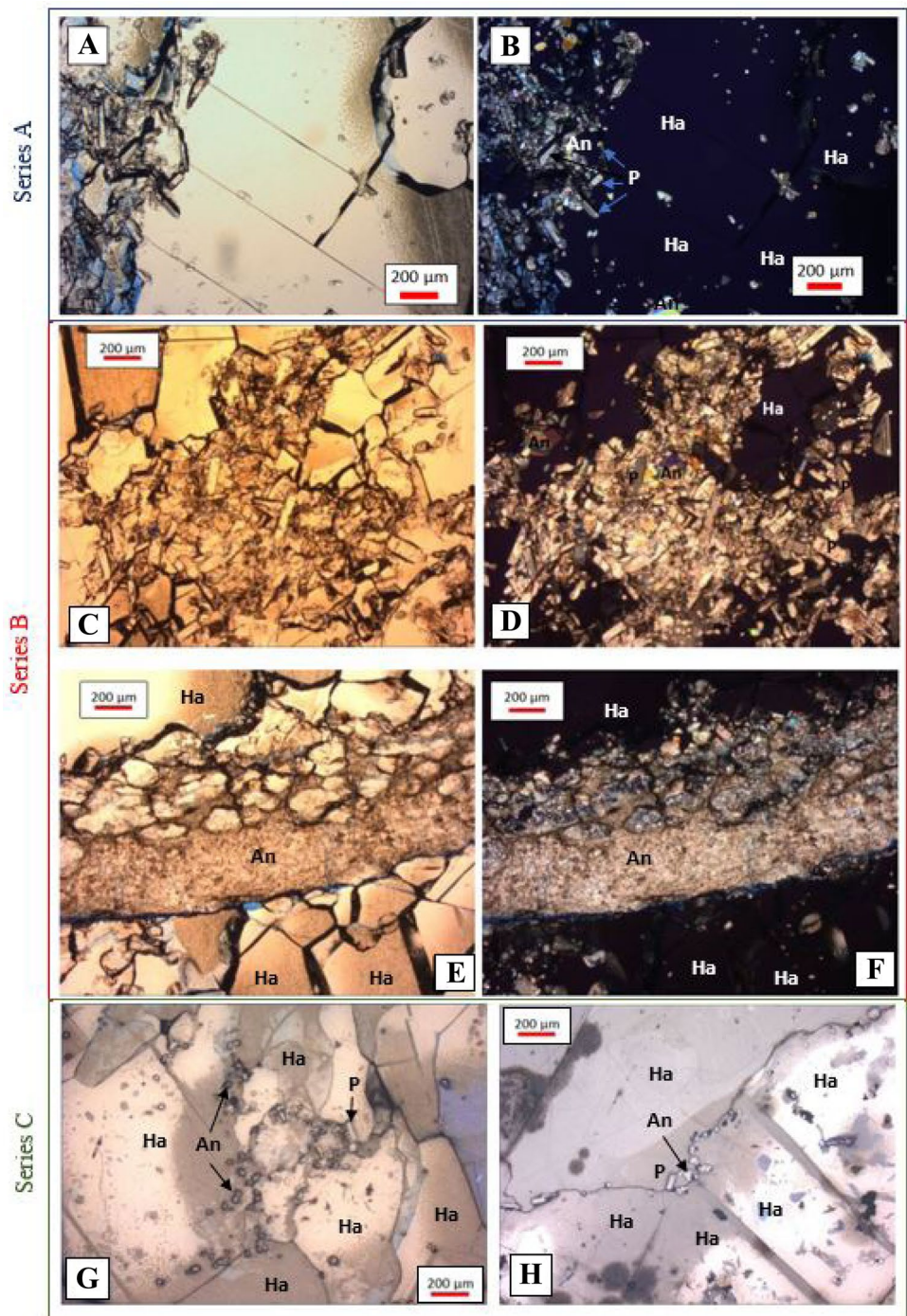
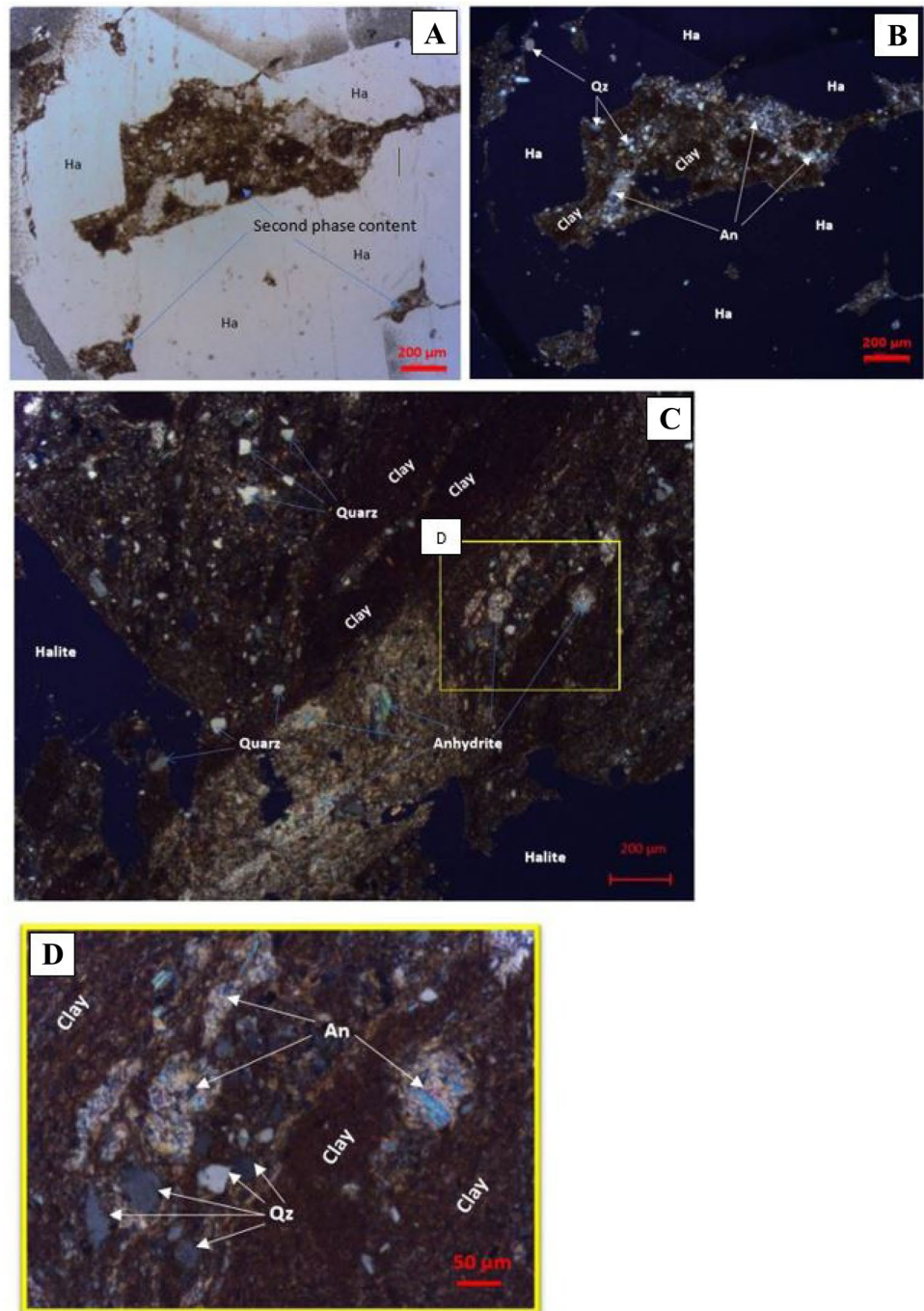


(Fig. 4a, b). Thin section analysis from samples collected from the two economically workable levels, zone B and zone F, shows aggregates of second-phase content with clay, anhydrite, and some grains of quartz located interstitially in bigger (1 mm–1.5 cm) halite crystals. Clay surrounding the halite crystals interstitially contains microscopic scale (10–80 μm) quartz grains and aggregates of anhydrite crystals with grain sizes from 10 to 200 μm (Fig. 4c). In Fig. 4c, a matrix of clay surrounding large (0.5–1 cm) halite crystals

can be observed (crossed polars). The clay mineral matrix contains 50 μm crystals of quartz and anhydrite aggregate crystals of around 50–100 μm . The aggregates show different morphologies, (i) circular aggregates with a radial distribution of anhydrite crystals, and (ii) individual elongated anhydrite crystals. No clear crystal orientation can be identified in the elongated aggregates. There are also 10–50 μm quartz grains. All grains of quartz and anhydrite crystal aggregates are held in a clay matrix.

Fig. 4 Microphotographs from Winsford Mine Layer B samples. **a** Aggregates of second-phase content with clay, anhydrite (An), and some grains of quartz (Qz) interstitially disposed in bigger halite (Ha) crystals. **b** Same view as A, but crossed polars. **c** Matrix of clay surrounding the large (0.5–1 cm) halite crystals. Crossed polars. **d** Close-up from area in c, showing aggregates of anhydrite crystals, with crystal sizes of 10–50 μm



Samples from LB series show a smaller mylonite–breccia grain texture (as defined by Leitner et al. 2011) with elongated crystal habit and grain size from 1 mm to 1 cm. The coloration of halite grains is orange-reddish to dark-brown, and shows similar texture as described to the mylonite haselgebirge with a strong content in halite, anhydrite, and mudrock (equivalent to clay) (Leitner et al. 2011; Othmar 1986). Figure 5a shows a thin section from LB series before deformation where strongly elongated and deformed halite grains indicating shearing can be

observed. Halite grain boundaries are strongly deformed with sinuous shapes. The main second-phase content observed is anhydrite and clay, both located mainly around the deformed halite grains. Some microcrystals of anhydrite can also be spotted interstitially enclosed within halite grains also containing fluid inclusions. Figure 5b shows the same section from A in crossed polars. A matrix of clay and microcrystalline anhydrite, with sizes from 10 to 50 μm , can be observed mainly distributed along halite grain boundaries.

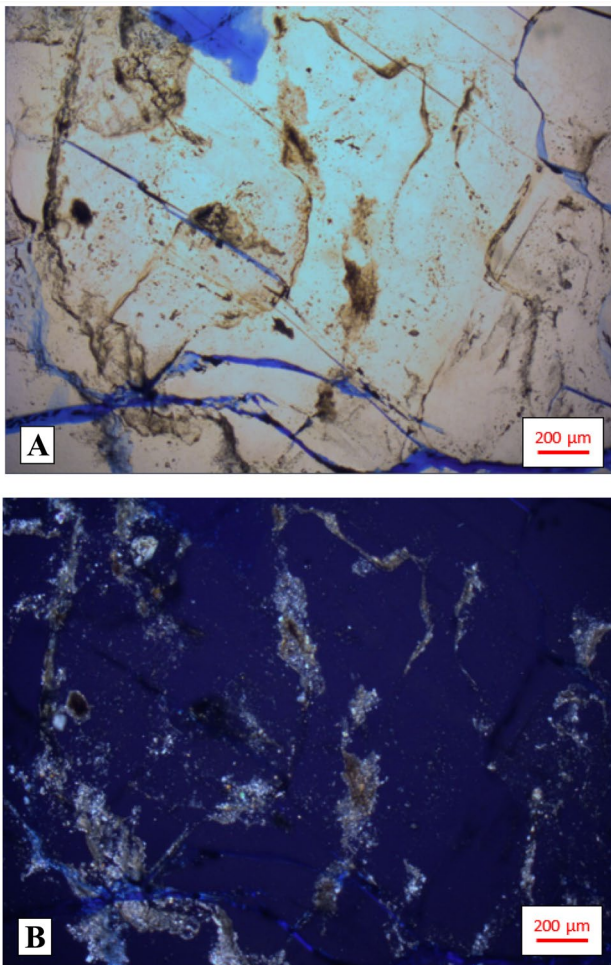


Fig. 5 Microphotographs from Winsford Mine sample LB4. **a** Thin section from sample LB4 under the transmitted light microscope. A mylonite–breccia grain texture can be observed with elongated halite grains with second-phase content (clay) observed along the grain boundary. Fractures can be observed across halite grains and halite grain boundaries. **b** Same view as **a**, but crossed polars. Second-phase content along grain boundary consists of a matrix of clay with microcrystals of anhydrite with crystal sizes of 10–50 μm

Signs of plastic and brittle deformation can be observed. Both inter- and trans-granular microfractures can be observed as highlighted by the epoxy blue resin in Fig. 5a.

5 Mechanical and Microstructural Results

5.1 Mechanical Data

Five different rock salt samples with different content in second-phase minerals were subjected to axial cyclic loading conditions between 4.5 and 7.5 MPa at 25 MPa of confining pressure and ambient temperature (22 – 25°C). Mechanical data (axial stress–strain and lateral strain

plots) and elastic parameters (Young’s modulus, Poisson’s ratio, Bulk modulus) are presented below. Although we do not explore the full linear elastic behavior of the samples nor quantify their full brittle failure, using the aforementioned elastic parameters allows us to measure the impact of the small microstructural changes that the mechanical testing conditions may induce from the evolution of the elastic response. The stress–strain data under cyclic mechanical conditions are reported in Fig. 6. We follow the convention that compressive stresses and compactive strains (i.e., shortening and volume decrease) are positive.

We first observe that (i) samples B8 and LB4 have a lower slope than samples A3, C3, and F4, and (ii) sample LB4 also recorded twice more axial strain than all the other samples. Sample A3 has a maximum axial strain $\epsilon_{\text{ax}} = 0.14\%$ at the last 7.5 MPa loading and $\epsilon_{\text{ax}} = 0.13\%$ at the last 4.5 MPa unloading. Sample C3 axial strain ranges from $\epsilon_{\text{ax}} = 0.11\%$ at 7.5 MPa and $\epsilon_{\text{ax}} = 0.09\%$ at 4.5 MPa. In comparison, sample B8 ranges from $\epsilon_{\text{ax}} = 0.17\%$ at the last 7.5 MPa loading and $\epsilon_{\text{ax}} = 0.15\%$ at last 4.5 MPa unloading. Both samples A3 and C3 also have a similar stiffness, whereas sample B8 shows a notably lower stiffness. Samples F3 and LB4 both recorded greater final axial strain compared to samples A3, B8, and C3 (Fig. 6). Sample F3 ranges from $\epsilon_{\text{ax}} = 0.18\%$ at 7.5 MPa and $\epsilon_{\text{ax}} = 0.16\%$ at 4.5 MPa. Sample LB4 has the greatest values of all samples with $\epsilon_{\text{ax}} = 0.31\%$ at the last 7.5 MPa loading and $\epsilon_{\text{ax}} = 0.28\%$ at last 4.5 MPa unloading. Sample LB4 also presents the largest initial axial strain during the first loading, highlighting its strong intrinsic inelastic behavior.

Lateral strain for the different tested rock salt samples along the cycles is presented in Fig. 7. Note that due to a technical issue on the circumferential strain gauge, unfortunately, no ϵ_{circ} data were recorded for sample A3. All sample curves first show a smooth negative logarithmic trend. Sample LB4 has recorded the least amount of lateral expansion (maximum $\epsilon_{\text{circ}} = -0.016\%$), whilst sample B8 the largest (maximum $\epsilon_{\text{circ}} = -0.062\%$). Moreover, we observe that sample B8 initially (within the first 1000 cycles) expands at a greater rate than the other samples. Between 1000 and 2500 cycle, overall, all samples’ ϵ_{circ} values decrease more slowly. Beyond 3000 cycles, the curves reach its near plateau value. Sample LB4 shows an increase in ϵ_{circ} up to 0.01% at about 500 cycles before continuing on its negative logarithmic trend till about 2500 cycles; then, it tends to a plateau till the end of the test. Sample F3 has a distinctive pattern of recurring variations in ϵ_{circ} on top of the logarithmic trend. Its lateral strain presents a quite fast increase in ϵ_{circ} during the first 1000 cycles up to 0.02% followed by a small positive recovery approximately every 200–500 cycles. Indeed, after 1000 cycles, several small positive recovery episodes in ϵ_{circ} can be observed in form of small jumps of -0.020 – -0.028% .

Fig. 6 Stress–strain curve for samples A3, B8, C3, F3, and LB4

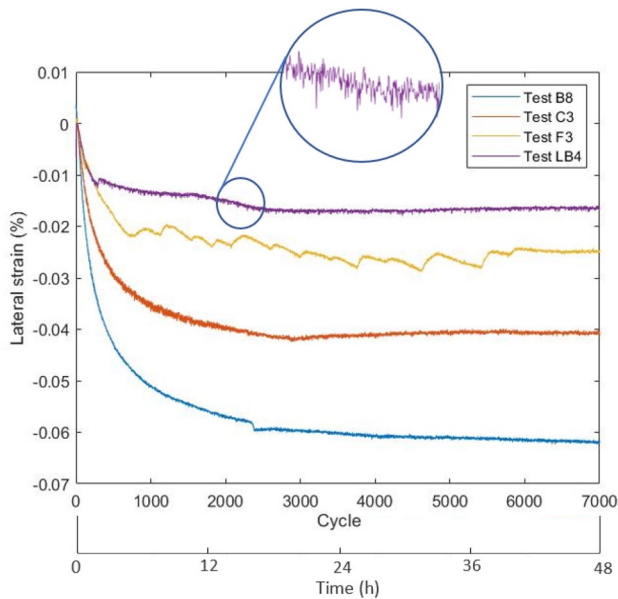
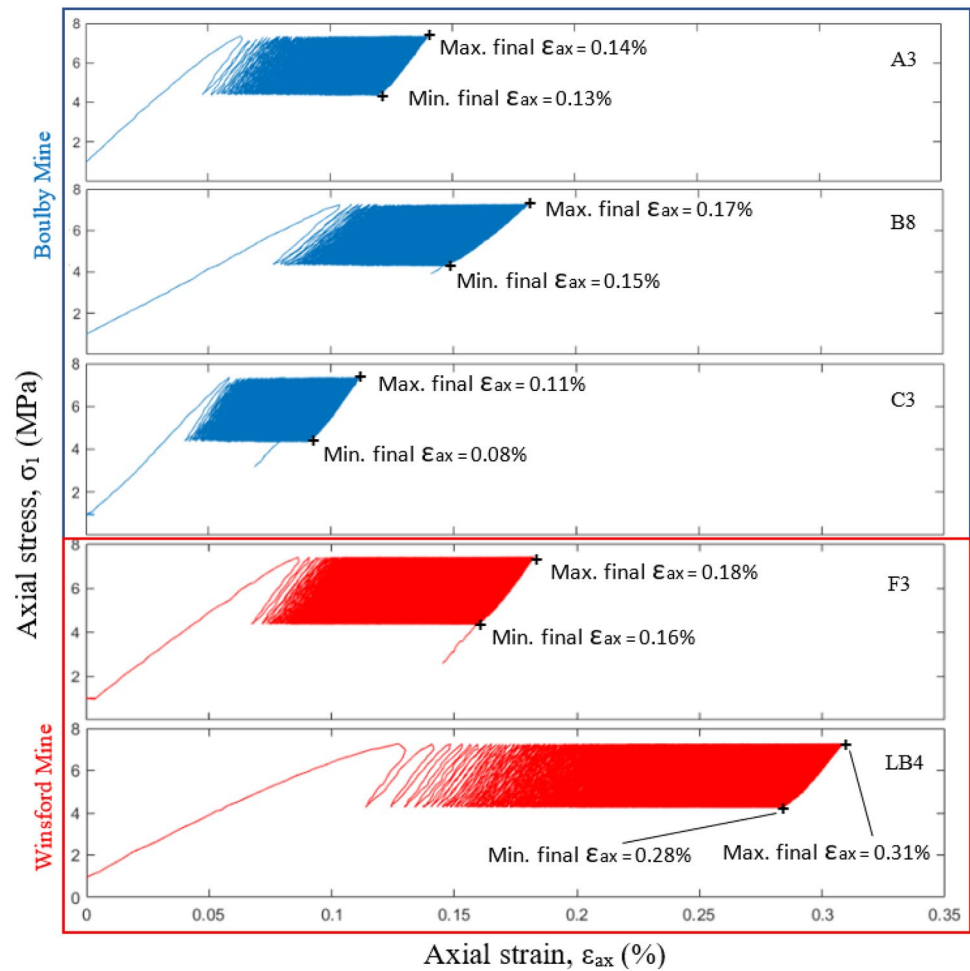


Fig. 7 Plot of ϵ_{circ} (%) against cycle number for all tested samples

Just before reaching 6000 cycles, the curve stabilizes with a slightly positive recovery to about $\epsilon_{\text{circ}} = -0.025\%$.

A slightly strain recovery can be observed in some samples. According to Berest (Berest 2011), even small thermal variations can generate thermo-elastic strains in pure halite samples (thermal expansion coefficient for rock salt is of $\alpha = 4 \times 10^{-5}/^{\circ}\text{C}$). This suggests that slightly changes in rheological behavior, like the jumps observed in sample F3 (Fig. 7), could be linked to involuntary small variations in room temperature. Hence, temperature changes during the cyclic mechanical loading experiment were recorded to account for any significant variation. Figure 8 shows the temperature evolution versus lateral strain. All tests show a decrease in temperature from the beginning of the test until the end with variations of temperature from $\pm 3^{\circ}\text{C}$ to maximum $\pm 5^{\circ}\text{C}$. Sample F3 is the sample showing the greatest temperature variation with a temperature drop of 4.5°C from the beginning (25.5°C) until the end (21°C) of the test. Despite F3 being one of the samples showing the least variation in lateral strain, the significant drop in temperature could be (between other factors like second-phase content) one of the reasons to explain why F3 show a

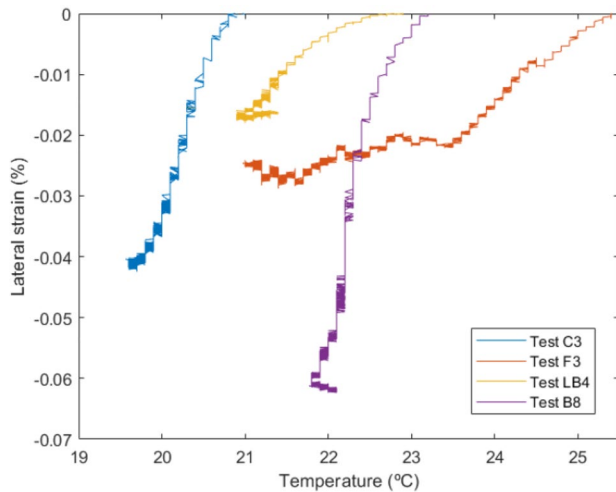


Fig. 8 Plot of ϵ_{circ} (%) against temperature during the cyclic loading mechanical test

repeated recovery in lateral strain around every 500 cycles. Even though thermo-elastic strains can play a significant role over creep rate in long-term creep tests in pure halite (Berest 2011), our data do not point to a clear relationship between the room temperature variations and the recorded strains during these short-term cyclic mechanical loading tests. The second-phase mineral content may also have allowed to accommodate this minor temperature effect differently.

5.2 Elastic Parameters

The Young's modulus (E) is calculated from the axial stress and strain data to analyse the changes in the elastic properties of the tested samples during the cyclic mechanical loading test. Figure 9 shows the individual cycle (noisy signal in light blue for samples A3, B8, and C3 and red for samples F3 and LB4) and average (overlying black curves on the blue and red signal) Young's modulus values as well as Poisson's ratio (black curves) value per cycle. Table 2 summarizes the recorded maximum and minimums of the average Young's modulus per cycle.

Overall, all tested rock salt samples show a softening process with a recognizable decrease in Young's modulus. Four out of five samples (namely A3, C3, F3, and LB4) show Young's modulus values between 13 and 16 GPa. Sample B8 has the lowest Young's modulus with $E \sim 9$ GPa. Sample B8 is also the sample that presents the lowest amplitude oscillation recorded regarding the elastic modulus in comparison to all the other samples. Samples A3, B8, and C3 record a marked decrease in Young's modulus value observed consistently between 2000 and 3000 cycles, with sample B8 having the smallest amplitude drop with just about 0.5 GPa of decrease. Samples F3 and LB4 also show a drop in

Young's modulus but during the first 500 cycles instead. Sample F3 has a more gradual decrease in Young's modulus along the first 1000 cycles, whereas sample LB4 shows a slightly positive jump in the first 100 cycles and then a more noticeable decrease between the first 100 and 500 cycles from 14 to 13 GPa. A slightly gradual decrease in the first 900 cycles can be observed in samples A3 and C3, but also a similar initial behavior in sample F3.

The Poisson's ratio (ν) does not change during the test period. Each sample shows a steady ν value ranging between 0.2 and 0.5%. Table 2 gives the mean value from Poisson's ratio calculated for each cycle. Samples F3 and LB4 show similar Poisson's ratio during the whole test. No Poisson's ratio was calculated for sample A3 due to the missing circumferential strain data, as explained above.

The Bulk modulus K can be calculated either from the Young's modulus and Poisson's ratio (Eq. 1) or also from the axial stress σ_1 applied and volume change of the sample (Eq. 2):

$$K = \frac{E}{3(1 - 2\nu)}, \quad (1)$$

$$K = \frac{\sigma}{\frac{\Delta V}{V}}. \quad (2)$$

Since no circumferential data (thus no Poisson's ratio) could be recorded for sample A3, sample A3 has no data for Bulk modulus. All the values are summarized in Table 2. The Bulk modulus remains steady across all the cycling tests, with values of about 23–24 GPa for all samples.

5.3 Microstructural Analysis

The microstructural modifications of the samples before and after the mechanical cyclic loading tests were analysed for samples A3, B8, and C3. Figure 10 shows petrographic images of samples A3, C3, and B8, before (on the left) and after (on the right) deformation.

Prior to the mechanical stimulation, we observed in all samples annealed structures of subhedral polygonal crystals with straight and strain free grain boundaries presenting 120° intersection. The thin section analysis shows halite crystals of between $500 \mu\text{m}$ and 2 mm diameter, lacking major fractures. Cleavage can be observed in the larger halite crystals. Minor microfractures within some second-phase minerals can also be identified sporadically, at a very low density and lacking connectivity.

After deformation, the microfracture network was drastically denser in areas with higher concentration in second-phase minerals. In general, the observed macroscopic axial shortening of the samples results from grain size decrease in the axial direction and subsequent grain size increase of the

Fig. 9 Young's Modulus and Poisson's ratio values for all samples

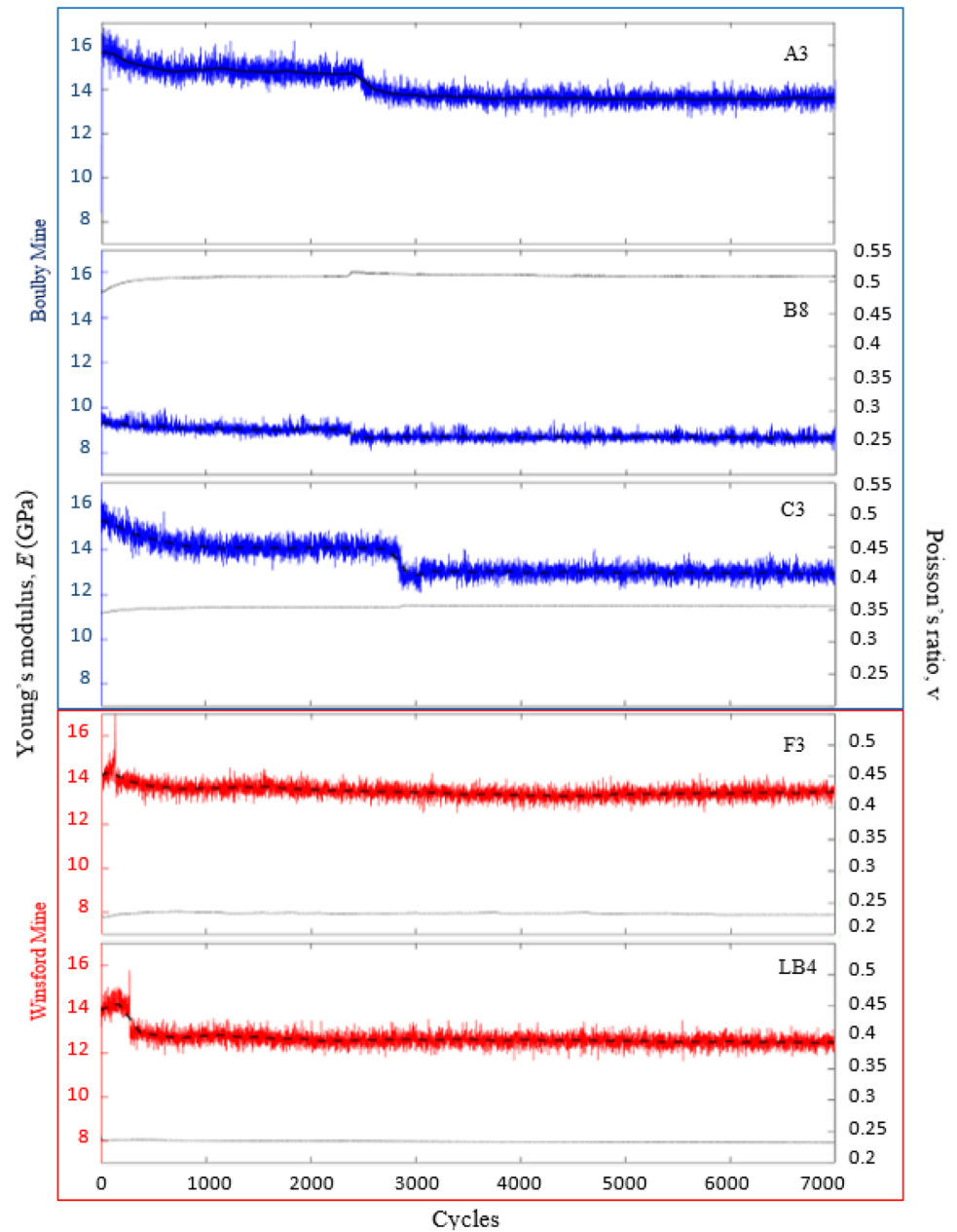


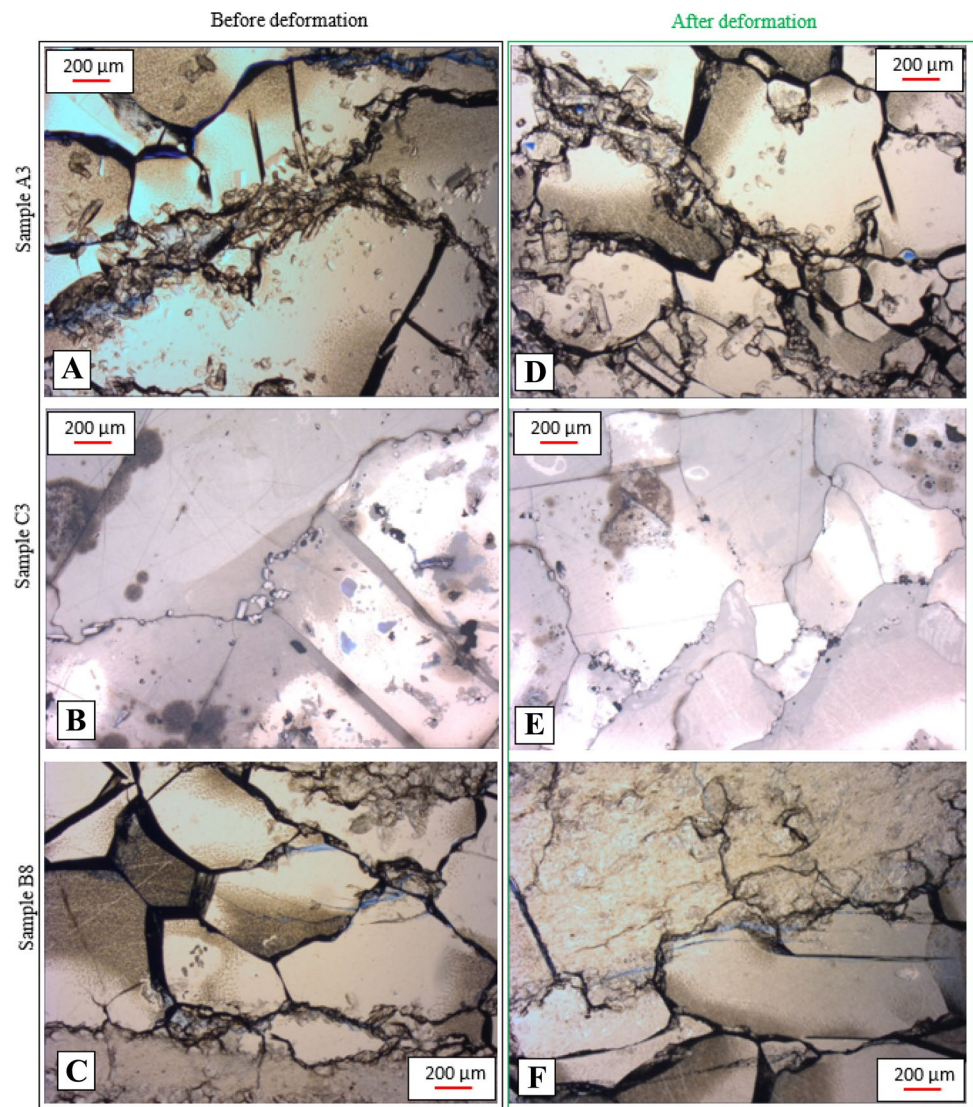
Table 2 Minimum and maximum values of the static elastic parameters for all tested samples

Sample origin	Sample ID	Young's modulus E (GPa)	Bulk modulus K (GPa)	Poisson's ratio ν
Boulby (Permian)	A3	13.5–15.6	–	–
Boulby (Permian)	B8	8.7–9.3	23.7–24.0	0.50
Boulby (Permian)	C3	12.8–15.3	24.6–24.8	0.35
Winsford (Triassic)	F3	13.3–14.3	24.2–24.3	0.23
Winsford (Triassic)	LB4	12.5–14.2	24.3–24.4	0.23

halite crystals perpendicular to σ_1 , in comparison to the pre-deformation subhedral shape of the halite crystals. The grain boundaries perpendicular to the maximum principal stress

σ_1 became more flattened after deformation. Halite crystals in sample A3 before deformation (Fig. 10a) are larger than 500 μm , whereas after deformation, the halite crystals are

Fig. 10 Microphotographs of samples A3, C3, and B8 before (a–c) and after (d–f) deformation



smaller, about 100 μm (Fig. 10d). Sample C3 shows similar grain size modification: a volume decrease from subhedral crystals with straight grain boundaries with high angle intersections of 120° (Fig. 10b) to more packed anhedral crystals showing curved and lobate grain boundaries (Fig. 10e). Figure 10f shows the microstructure from B8 after deformation with a clear increase in microcracking linked to areas with a higher content in anhydrite and boundary flattened on grain boundary perpendicular to σ_1 resulting in a halite grain elongation. Overall, this sample recorded the highest degree of damage due to microfractures that developed within the anhydrite minerals.

The microstructural analysis of samples F3 and LB4 also shows a slightly decrease in grain size compared to the reference intact materials. The deformation mechanism is observed around halite grains and appeared to be related to a higher anhydrite and clay content. Figure 11 shows the microstructure of samples from series LB and F before

(Fig. 11a, b) and after (Fig. 11c, d) the cyclic mechanical loading test. Due to the significant pre-existing microstructural damage in series LB, it is difficult to clearly distinguish the deformation structures before and after the test. Nonetheless, we noticed some increase in deformed structured similar to dislocation creep following halite cleavage and a decrease of halite grain sizes, related to area with a greater content in anhydrite and clay around grain boundary. However, we cannot certify these structures were produced during the cyclic loading mechanical test.

The analysis using the scanning electron microscope (SEM) shows new pores being generated around some second-phase minerals in sample A3 as a result of mineral rotation (as highlighted by green arrows on Fig. 12b). The mineral rotation also induced (i) grain boundary opening (Fig. 12a) and (ii) some microfracturing between anhydrite crystals, as indicated by magenta arrows in Fig. 12c.

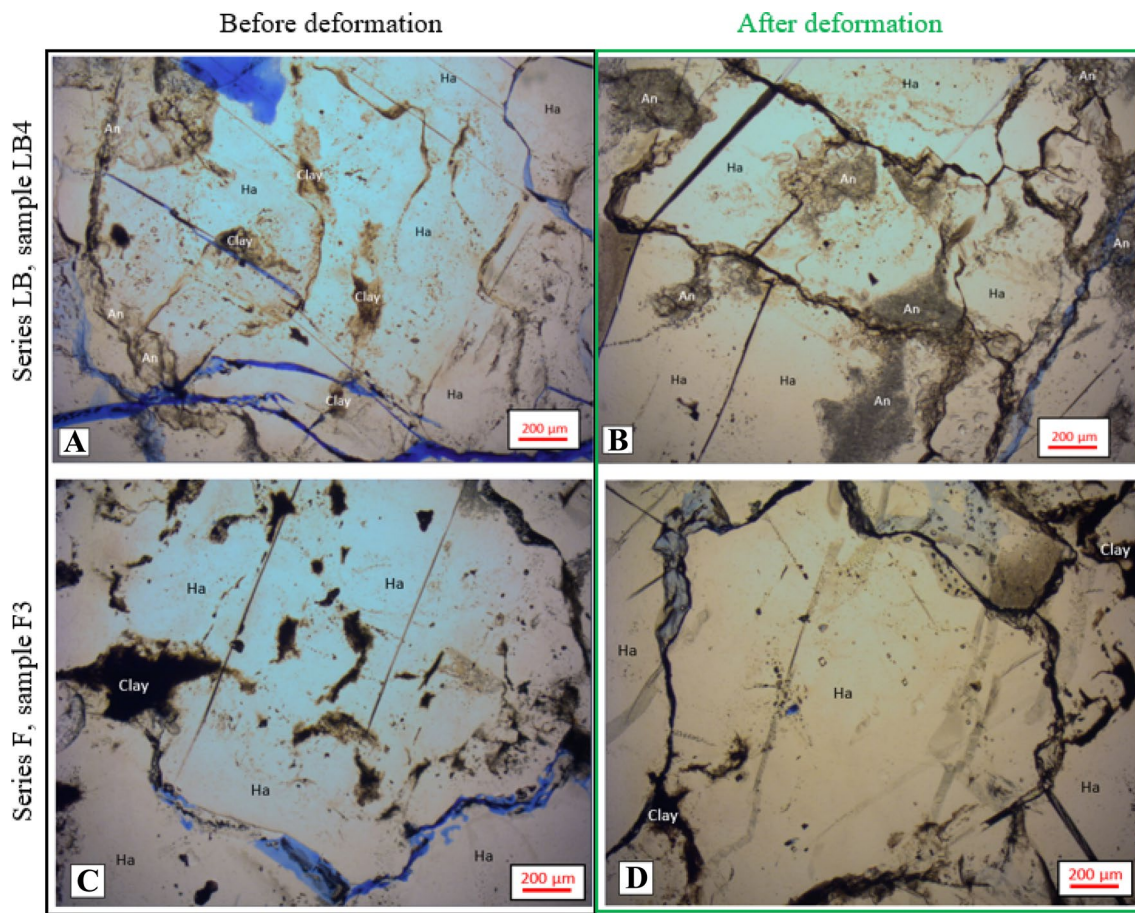


Fig. 11 Thin section analysis of samples LB4 and F3 before and after deformation under cyclic loading conditions. A slightly decrease of halite (Ha) grain size can be observed. Second-phase content along grain boundary consists of a matrix of clay with microcrystals of anhydrite (An)

6 Discussion

6.1 Impact of Second-Phase Content on Elastic Parameters

We can observe in Fig. 6 (stress–strain curve) that the sample with the highest final strain is LB4 followed by F3 and B8 with very similar final strains. This difference in maximum final strain can be explained not only for the mineralogical content but also the texture. According to Hickman and Evans (1995), Martin et al. (1999), Spiers and Schutjens (1999), and Lohkämper et al. (2003), the presence of mudrock (assumed to be similar to the clay content of our sample here), and other second-phase content, can induce enhanced pressure solution of halite and hydrofracturing of mudrock when there is also the presence of water in the system. A greater amount of clay in samples from Winsford Mine would thus explain larger final axial strains for those samples in comparison to samples from Boulby mine (A3 and C3) despite same content of halite. Moreover, the breccia-haselgebirge texture from LB4 (in addition to

the presence of clay minerals) would explain the dramatic increase in maximum amount of axial strain in comparison to the rest of the samples presenting a nonclastic-crystalline texture. Pre-existing fractures, previous to the cyclic mechanical loading test, have also likely played an important role in accommodating the axial shortening of sample LB4. Figure 13 shows the values of Young's modulus (top graphs) and maximum ϵ_{ax} recorded per cycle (bottom graphs) per cycle for all samples. The ϵ_{ax} recorded per cycle is the peak ϵ_{ax} recorded at the maximum principal stress applied (σ_1) of 7.5 MPa every cycle. The orange bands mark the transition from stage I to stage II in which a change in the curve trend is observed and the marked drop in Young's modulus values is recorded in samples A3, B8, and C3. Samples LB4 and F3 also present the same trend, but the decrease occurs much earlier, during the first 500 cycles. This change in rheological behavior, implying a strain recovery of around 0.01–0.02% (for samples A3, B8, and C3), seems to be related to the transition between two different deformation stages as captured by the plot ϵ_{ax} versus the number of cycles in samples A3, B8, and C3: typically, the axial strain first

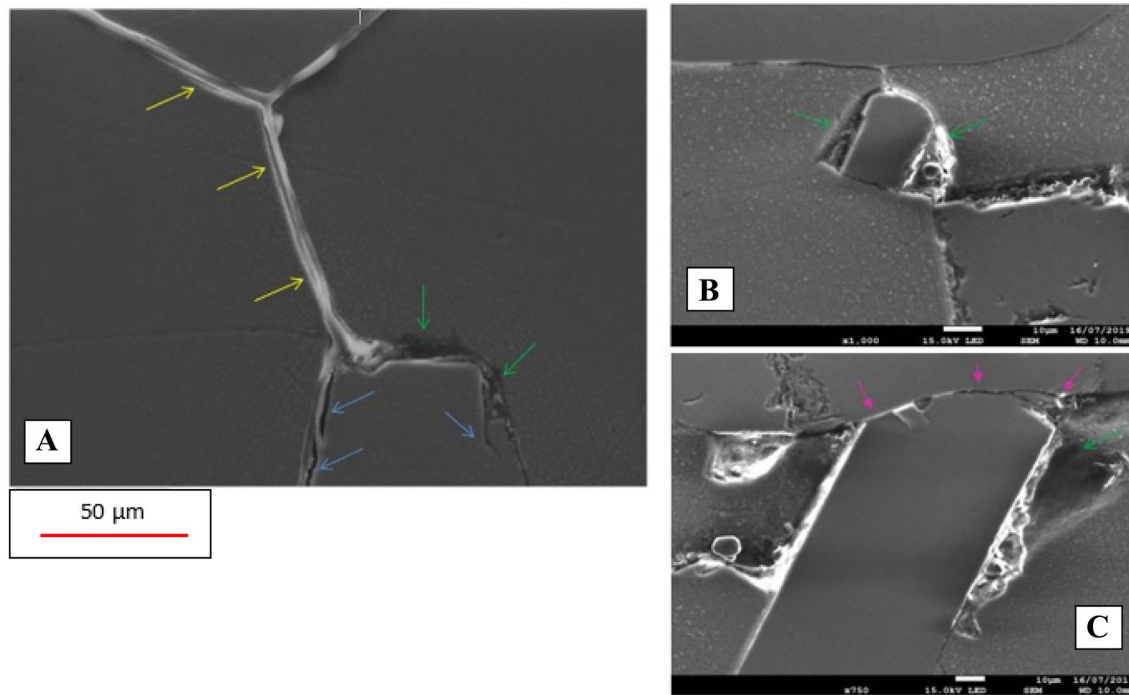


Fig. 12 SEM images of sample A3 after deformation. Porosity generation (green arrows) can be observed as a result of second phase mineral rotation under cyclic mechanical loading. Yellow arrows mark the boundary opening at the halite–halite contact and the blue arrows

indicate the grain boundary at the halite–anhydrite contact. Purple arrows show plastic deformation between two grains of second-phase content as a result of grain rotation during the cyclic mechanical loading test (Color figure online)

increases to reach a short plateau period before diminishing whilst the cyclic loading continues. After few hundreds of cycles, it increases again steadily until the end of the test (Fig. 13 bottom). Samples A3 and C3 have similar magnitude of changes, whilst sample B8 axial strain variation has a much smaller amplitude. Further investigation will be needed to clarify the changes in rheological behavior (described in this paper as two different deformation stages) in relation to the strain recovery only observed in samples from Boulby Mine (A3, B8, and C3).

Inhomogeneous deformation has been studied in other materials such as metals and alloys, where inhomogeneous creep observed recorded in strain-time data is associated with shear bands before creep and the presence of pre-deformation microstructures (Li 2015). Shear deformation is observed here in the corresponding thin sections of our post-deformation samples (Fig. 14). However, to capture the microstructural changes at this particular period, some experiments should have been stopped just before 2000 cycles and others just after 3000 cycles, under same the cyclic mechanical loading conditions. Since we only recovered the samples after 7200 cycles, more damage has very likely overprinted the one that occurred at this stage. More work is thus necessary to improve our understanding of the deformation mechanisms and internal structural changes linked to this notable change in mechanical properties.

Voznesenskii et al. (2017) also recorded a decrease in dynamic Young's modulus—calculated from ultrasonic velocity surveys—during cyclic loading conditions of similar amplitude, with a subsequent increase after more cycles were applied. The decrease in Young's modulus and rock sample strength was interpreted as a result of inner material arrangements. Our data also captured a similar decrease but after a larger number of cycles (after few thousands instead of just about 20 cycles). No subsequent static Young's modulus increase was observed however. According to Voznesenskii et al. (2017), two opposite processes are taking place during cyclic loading: first dilatation, as the result of halite grain displacement relative to each other; second consolidation, accompanied by compaction, with a decrease of grain size and intergranular porosity, caused by salt diffusion at the grain boundaries. However, although a slightly decrease in grain size has been observed in thin sections after deformation, none of the rock salt samples tested showed an increase in Young's modulus.

The Poisson's ratio (ν) is 0.35 for sample C3, 0.5 for B8, and 0.23 for samples F3 and LB4 (Table 2). Although Poisson's ratio values of 0.20–0.25 are common for rock salt, values up to 0.40 have also been reported in rock salt studies and used for rock salt rheological behavior modeling (Li and Urai 2016; Senseny et al. 1992; Liang 2007). Poisson's ratio also shows a slightly variance linked to the drop observed in

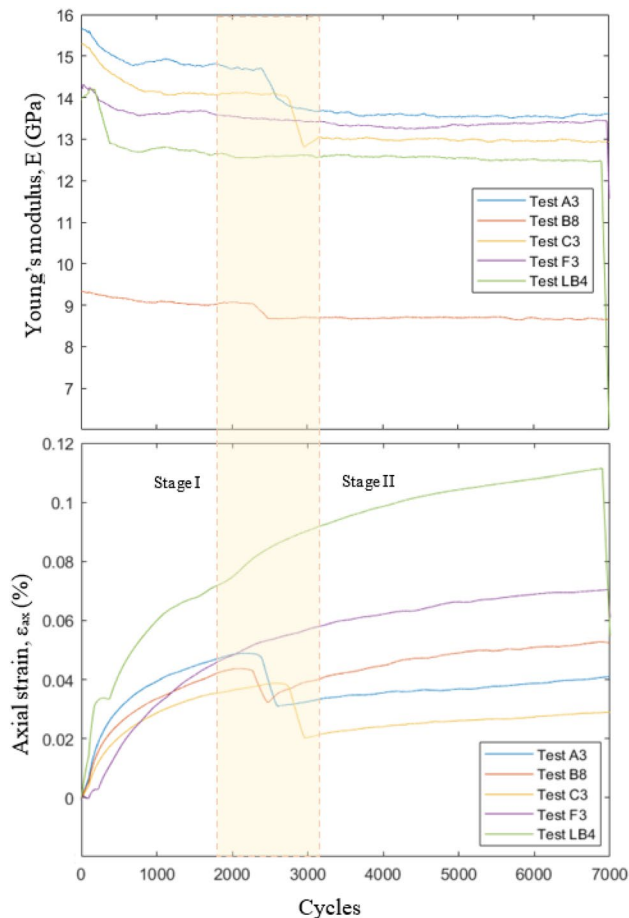


Fig. 13 Plots of Young's modulus variation and of strain against cycle number for all samples. The orange band indicates the lapse between 2000 and 3000 cycles where a drop in Young's Modulus value and transition from stage I to stage II occurs simultaneously (Color figure online)

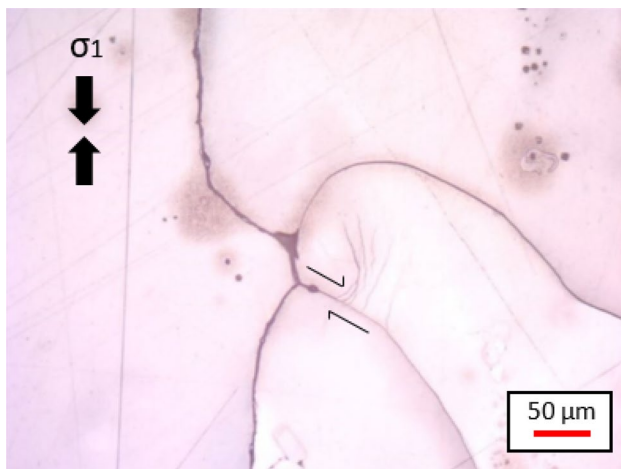


Fig. 14 Image in the transmitted light microscope from C3 after deformation. Shear deformation is observed in halite grains. Principal stress σ_1 is represented with black arrows on the top left of the picture

Young's modulus (Fig. 9). Taken together, the lowest value of Young's modulus and highest value of Poisson's ratio calculated for sample B8 seem to highlight that the outstanding microstructure (low halite content, high second-phase content) of this sample compared to the others is significantly impacting the mechanical properties of such rock salt.

6.2 Deformation Mechanisms in Rock Salt

Rock salt can accommodate deformation via a large range of mechanisms. Many mechanisms, from dislocation creep to pressure solution and dynamic recrystallisation, have been studied for decades. Although an increase of mechanisms similar to pressure solution can be observed here in the tested samples with a high second-phase content, such as anhydrite and polyhalite, a more detailed review of the constitutive laws is needed to fully distinguish between previous internal structures and deformation induced by the cyclic mechanical loading test. Dislocation creep mechanism, which takes place within the crystal lattice, dominates deformation on short duration laboratory tests at a high range of temperatures (100–200 °C) (Urai and Spiers 2007; Li et al. 2012). Solution-precipitation creep, which take place in the grain boundaries, and dynamic recrystallisation play an important role in long-term deformation processes (Li et al. 2012). During dislocation creep, if the halite grains contain significant amounts of water in fluid inclusions or in the grain boundary, fluid-assisted grain boundary migration occurs by solution-precipitation transfer across grain boundary water/brine films. This helps to decrease dislocation density and remove the stored energy from dislocations (Urai and Spiers 2007; Schenk and Urai 2004; Schenk et al. 2006). Also, during pressure solution, highly stressed boundaries dissolve allowing the diffusion of material through grain boundary fluid which crystallizes under low normal stress (Urai and Spiers 2007; Spiers and Schutjens 1999). Compaction of porous salt may occur as result of a grain rearrangement by the intergranular sliding and rotation processes accompanying pressure-solution process (Spiers and Schutjens 1999).

Several factors such as temperature, confining pressure, grain size, second-phase content, and the presence of brine water in grain boundaries will determine the relative importance of those processes during rock salt deformation (Urai and Spiers 2007). Although solution-precipitation creep has been described in several laboratory investigations, with temperature ranges of 20–200°C (Urai et al. 1986; Urai and Spiers 2007; Berest et al. 2005; Spiers et al. 1990; Spiers and Brzesowsky 1993; Renard et al. 2002, 2004) due to the strong dependence of grain size and limited duration of laboratory tests, it is difficult to observe this deformation mechanism in experiments on natural rock salt at laboratory time scale (Urai and Spiers 2007).

Urai and Spiers (2007) and Li and Urai (2016) conducted a data recompilation from previous analysis on rock salt samples tested at constant load in the literature. This data has been used in this paper for a better understanding of the deformation processes taking place during the cyclic mechanical loading test. Although previous laboratory research on deformation mechanisms in rock salt has been conducted under constant stress deformation, we observed that rock salt samples deformed at a low range of cyclic mechanical loading conditions still presents a similar behavior to the typical creep behavior observed in

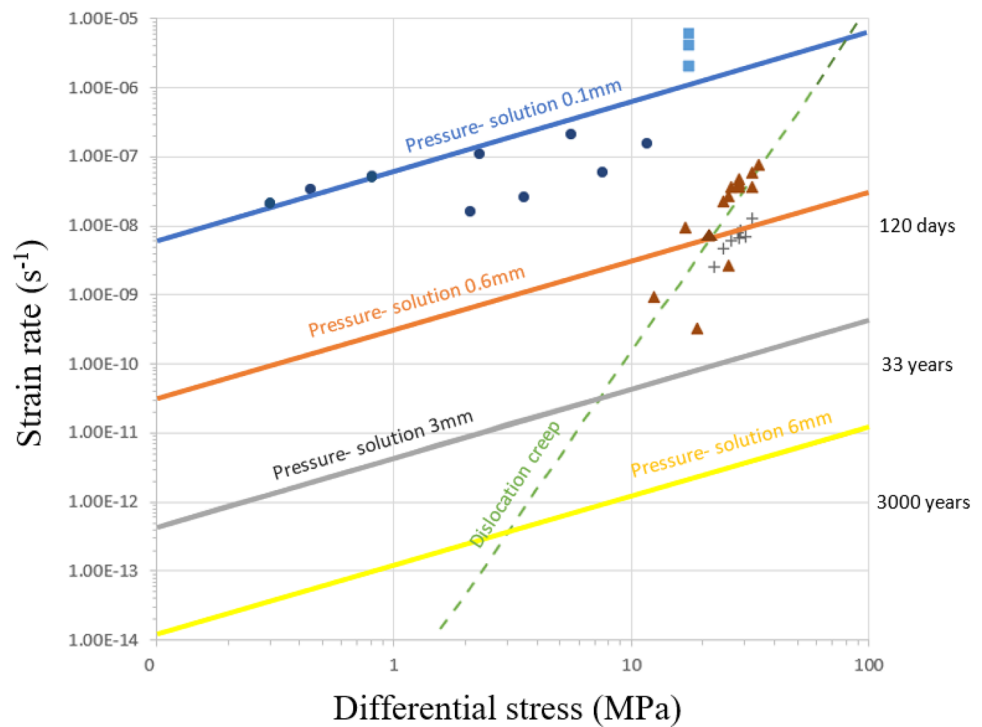
strain–time plots under a constant stress, where it can be distinguished an initial stage (stage I) and a steady-state stage (stage II). For this reason, we calculated steady-state strains from strain versus time plots (Fig. 13). Steady-state strain rates for all samples and the differential stress are summarized in Table 3. The plotted results correspond to the data recorded at maximum axial stress applied (7.5 MPa) during the mechanical loading test and also showed in Fig. 13.

Figure 15 presents the differential stress–strain rate diagram with the data from all samples tested at the maximum axial stress applied during the cyclic mechanical loading test (represented in blue squares) and recompiled data from the literature review (Urai and Spiers 2007; Li and Urai 2016; Schleéder and Urai 2005). Discontinuous line represents extrapolation of the dislocation creep law. Solid lines are the room temperature solution-precipitation creep law in different colors for different grain sizes (after (Urai and Spiers 2007; Schleéder and Urai 2005)). Creep constitutive laws help to predict and model deformation processes under certain mechanical conditions. The graph shows that, with the strain rates calculated at the steady-state stage of the strain versus time plot, our samples are below the domain

Table 3 Steady-state strain rate values for all samples

Sample origin	Sample ID	Strain rate (s ⁻¹)	Differential stress (MPa)
Boulby (Permian)	A3	2.00e-06	17.5
Boulby (Permian)	B8	4.00e-06	17.5
Boulby (Permian)	C3	2.00e-06	17.5
Winsford (Triassic)	F3	4.00e-06	17.5
Winsford (Triassic)	LB4	6.00e-06	17.5

Fig. 15 Strain rate (s⁻¹) versus differential stress (MPa) plots for all tested samples and a summary of data from previous tests from the literature review (After (Urai and Spiers 2007))



Previous laboratory data collected from different authors (after Schleeder & Urai, 2005; Spiers and Urai, 2007)

- Fine grained wet halite
- ▲ Coarse grained halite
- + Coarse grained halite

■ Rock salt tested at room temperature (22-25°C) under cyclic conditions.

of pressure–solution for samples with a grain size of 0.1 mm. Thus, lower strain rates would be needed for pressure–solution between halite grains to take place in a sample with a grain size from 0.5 mm to 1.5/2 cm. Hence, although pressure–solution structures can be observed in rock samples after deformation, it is not possible to certify that those structures are a result of the cyclic loading mechanical deformation. Figure 15 not only evidences that slower strain rates are required to meet pressure–solution at those grain sizes but also longer testing times than 48 h.

6.3 Elastic Recovery Capacity in Rock Salt

The stress–strain plots shown in Fig. 6 recorded the minimum and maximum ϵ_{ax} for each minimum and maximum axial stress applied per cycle. Every cycle was loading up to 7.5 MPa and then unloading to 4.5 MPa. Therefore, during every cycle, the samples recorded an elastic recovery where the ϵ_{ax} at maximum axial stress registers a positive recovery when the sample is unloaded. The difference between the maximum ϵ_{ax} and the minimum ϵ_{ax} per cycle is interpreted here as the elastic recovery capacity of the sample. Hence, the total deformation of the sample is the sum of the initial deformation by the static load until 4.5 MPa and the creep and damage deformation induced by the cyclic loading test (Zhenyu and Haihong 1990).

Figure 16 shows the evolution of the elastic recovery capacity during the cyclic tests for all samples. All graphs present a positive trend, with two distinctive patterns observed. Samples A3, B8, and C3 values vary along the cyclic testing, with local increase, decrease, or steady periods. Samples F3 and LB4 do not show significant changes for the duration of the test. Only sample LB4 shows a noticeable increase during the first 500 cycles before reaching a plateau value of elastic recovery capacity.

Elastic deformation in rock salt is linked to interatomic forces resisting the distortion produced over the crystal lattice when a stress is applied and then removed, bringing the lattice to the equilibrium position at zero stress. Inelastic deformation is permanent and non-recoverable deformation as a result of line motion from imperfections in the crystal (dislocations), mass diffusion, and, at low pressure, microcracking (Senseny et al. 1992). Sample B8, with the highest second-phase content and lowest halite content (60%), shows a higher elastic recovery capacity per cycle than every other tested samples that have a higher halite content in comparison (more than 80%; Fig. 16). Indeed, all samples but B8 show elastic recovery values between 0.018% and 0.024%, whereas B8 has an elastic recovery value of around 0.03%. The most notable increase in the elastic recovery capacity for samples A3, B8, and C3 is registered between 2000 and 3000 cycles, simultaneously with the drop in Young's modulus and the change in strain versus cycle number. In

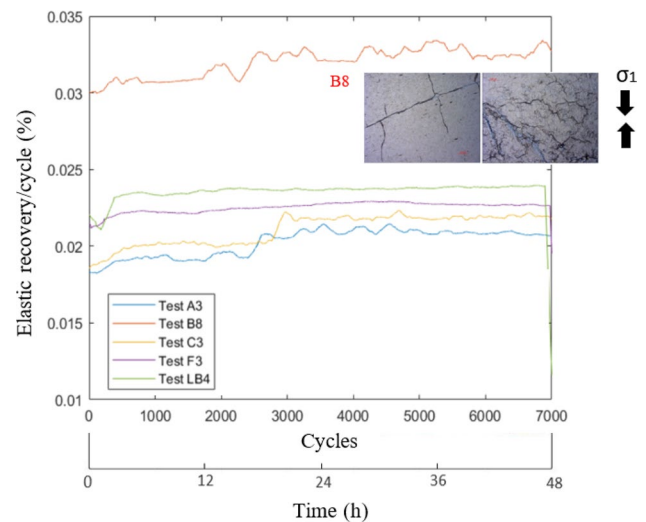


Fig. 16 Plot of the elastic recovery capacity variation against cycle number for all samples. Sample B8 shows a higher elastic deformation in comparison to the other samples. Two petrographic images from sample B8 present the fracture network in the anhydrite layering after deformation with microcracking as the main deformation mechanism in sample B8. The micrograph from sample C3 displays pressure solution, resulting in a more plastic deformation. A schematic picture of pressure solution creep summarizes the main deformation structures from this deformation mechanism (after (Urai and Spiers 2007))

comparison, samples F3 and LB4 show very stable elastic recovery values of around 0.022–0.024%. Based on post-deformation petrographic analysis, sample B8 shows a major formation of microcracks during the cyclic loading test. Several authors have investigated the relationship between the effects of differential, effective stress and temperature over permeability of rock salt [Urai et al. 1986 (17), Peach and Spiers, 1993 (add), Peach et al. 2001 (add), and Popp et al., 2001 (add)]. Rock salt permeability can dramatically increase when tested at low effective stress and low temperatures by microfracturing and dilatancy. However, the higher concentration of microfractures, in the samples analysed, is linked to the anhydrite bands between halite layers in the sample (see corresponding inserts micrographs from the transmitted light microscope in Fig. 16). We propose that the microcracks could act as sliding paths assisting the elastic recovery during axial stress unloading, thus supporting sample B8 higher elastic recovery in comparison to the other samples. The variations observed on the elastic recovery graphs for samples A3, B8, and C3 could be also linked to the polyhalite presence as a second-phase minerals.

Elastic recovery curves for samples A3, B8, and C3 show higher variation along the whole test, while samples F3 and LB4 show a smoother trend. All samples A3, B8, and C3 have polyhalite as a second content mineralogy which is harder than anhydrite (Pfifle and Senseny 1981). The

present of polyhalite as second-phase content could be an explanation for a higher variability in elastic recovery along the cyclic mechanical test.

The thin sections after deformation suggest that most plastic deformation newly observed is driven by a decrease in halite grain size which could be accompanied with grain boundary diffusion in halite crystals. Deformation of rock salt under low-stressed conditions is mainly controlled by pressure-solution creep, involving crystal grain slide with pressure solution and dynamic re-crystallization processes (Urai and Spiers 2007; Berest et al. 2005). However, the comparison of our data to other data from the literature suggests that strain rates reached during the cyclic mechanical loading test performed are neither slow enough nor long-lasting in time for pressure-solution creep mechanisms to take place. Small shear deformation traces in halite crystals, observed in sample C3 after deformation, could be related to defects of crystal misorientation and grain boundary sliding (Fig. 14). Deformation of grain boundaries in Fig. 14 could have been a result of rotation re-crystallization or boundary rotation (Drury and Urai 1990) as does the observation of many rocks with 120° triple junction (Urai et al. 1986). As a result of this rotation and the crystal misorientation, plastic deformation appears in the form of plastic microfractures with a very low angle from the direction of σ_1 applied (horizontal) during the cyclic loading test. Grain boundary migration seems to be observed in Fig. 17a, where material from a halite grain enters in the neighbouring grain boundary and recrystallizes on the lattice of that grain (Urai et al. 1986).

6.4 Brittle Damage and Porosity Enhancement Induced by Deforming Rock Salt Minerals

A clear relation between microcrack formation and higher second-phase content has been already discussed. The main deformation mechanisms in areas with higher concentration in second-phase content is microcracking and grain size decrease (Fig. 17). This creates new porosity.

Deformation and damage around halite grains can also be observed as trans-granular microcracking (TMC) in the presence of second-phase content. second-phase content acts as a weakening agent in halite crystal deformation (Fig. 17c). Sample B8 also shows fluid inclusions arranged along linear disposition across some halite grains. According to Urai (1983), during grain boundary migration, fluid inclusions encountered are incorporated to the thin fluid layer promoting the migration. When the grain boundary is pinned due to the presence of second-phase content, fluid inclusions can be left behind resulting in an array of fluid inclusions.

According to Schulze et al. (2001), both permeability and porosity depend on the state of stresses, the differential stress relative to the dilatancy boundary, and on the principal minimum stress. Strain accumulation during mechanical

loading and the distribution of hard particles can imply crack patterns and permeability to develop anisotropically, with orientations that depend on load geometry. SEM analyses have shown that other types of damage related to the cyclic mechanical loading can occur by mineral rotation. In spite of an increase of porosity around isolated grains of anhydrite due to crystal rotation under cyclic conditions, there is no evidence here of an increased permeability as the new porosity generated does not show further connectivity with other microfractures. However, we can observe an important increase in microfractures connectivity linked to anhydrite layering that could result in a potential increase in rock permeability. A high concentration of such second-phase mineral content could thus support the creation of a connected microfracture network capable to impact the transport properties of a rock salt volume.

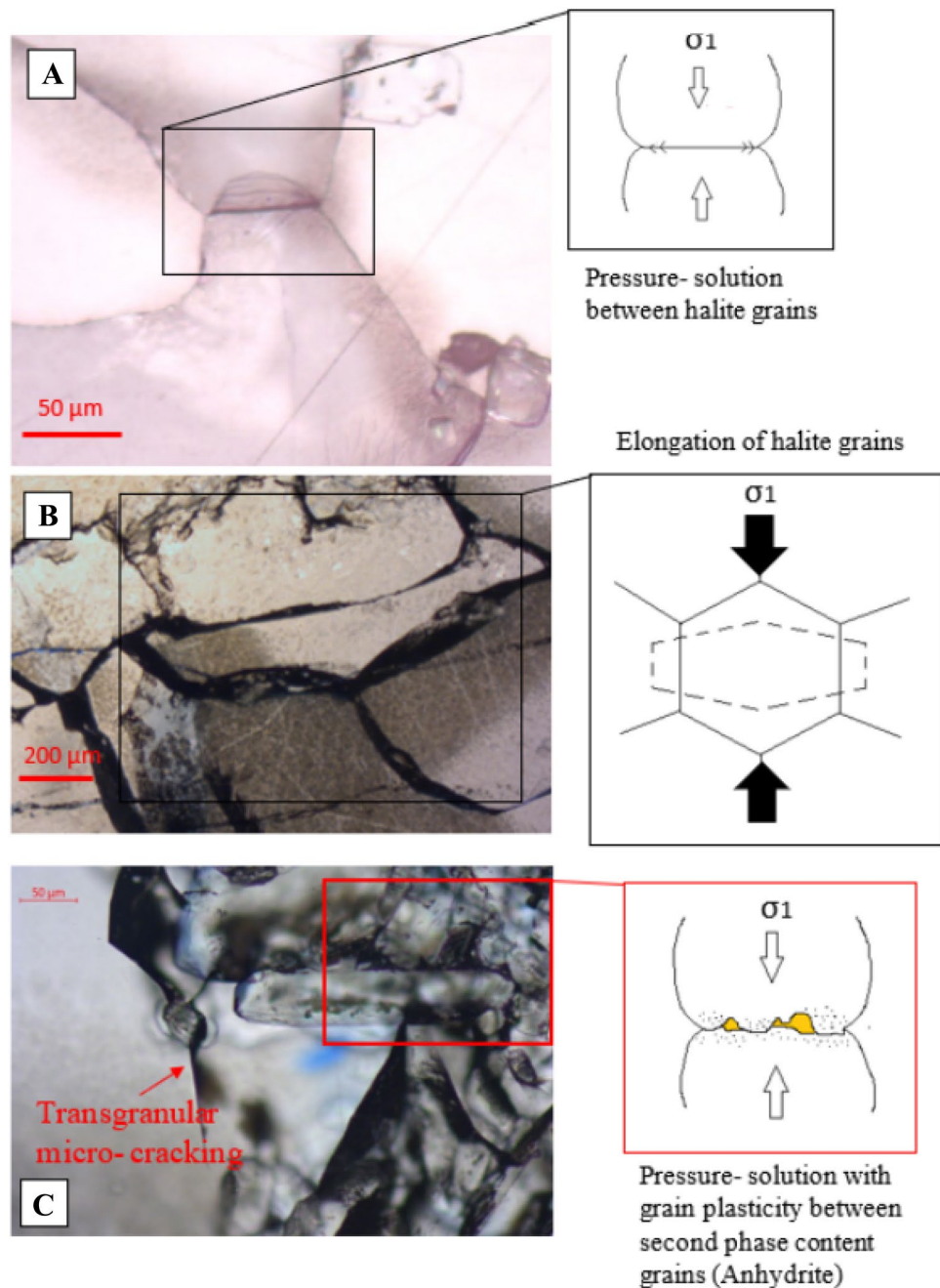
Grain size decrease is observed in all samples, where spherical-like crystals are changing shape to more elongated crystals. An example of this can be seen in deformed sample B8 (Fig. 17b), with a micrograph showing a vertical shortening accompanied by an horizontal elongation of halite grains.

6.5 Implication of second-phase content for UGS Safety

Several authors has investigated the compressibility and strain rate evolution of salt caverns to predict salt cavern closure on both long and short terms based on numerical modeling and in situ monitoring data (Brouard 2013; Moghadam et al. 2013; Wang 2013; Moghadam 2015; Wang 2016). A study from Brouard (2013), analysing in situ elastic parameters from the salt cavern at Gellenoncourt (France), states that long-term subsidence and possible brine leaks from the cavern should not have an environmental impact. However, none of the previously cited studies consider the impact of secondary minerals in rock salt cavern stability in their models (Brückner et al. 2003). By testing samples with different second-phase content at the same conditions, we have observed how a higher amount of anhydrite content for instance can result in higher strains under differential stress accompanied with an increase in brittle deformation and greater connectivity of the microfracture network.

Rock salt can also creep at high strain rates without showing brittle deformation and tends to self-heal (Wawersik and Preece 1982). However, microcracks along secondary mineral layers, such as anhydrite, in bedded salt can cause integrity problems, resulting in a gas leak through the formation due to a lower self-healing capacity of anhydrite in comparison to rock salt (Beauheim et al. 1993; Pluymakers and Niemeijer 2015). Interlayered composite rock salts are more common than pure halite thickened salt formations where secondary mineralogy will act as a weakening agent

Fig. 17 Microphotographs and sketches of main deformation structures observed as a result of pressure solution creep. **a** Sample C3 after deformation. Pressure solution between two grains of halite is observed. The sketch on the right shows the principal axial stress applied. **b** Sample B8 after deformation, showing a decrease and horizontal shortening of halite grains. The schematic diagram on the right displays how crystals undergo axial shortening and giving as a result of halite grain elongation. **c** Sample A3 showing the main deformation mechanisms implied in a more brittle deformation in relation to the presence of second-phase content. The main structures described are trans-granular microcracking with grain plasticity. The sketch on the right shows porosity generation (represented in yellow) along the grain boundary between two grains of anhydrite (Color figure online)



(Liang 2007). The structural analyses of samples A3, B8, and C3 after deformation have shown that the layers of anhydrite present the highest concentration of new microfractures after 48 h of cyclic mechanical deformation. Hence, we can see a clear relationship between an increase in anhydrite content and the creation of new microfractures under cyclic mechanical loading. This implies that even low operation pressure changes inside salt caverns could lead to significant damage propagation throughout the entire cavern walls as well as potential reduction of the cavern's volume (Han et al. 2006) as a result of the amount of second-phase content.

More investigation is needed to fully understand the micromechanisms leading to brittle deformation on the long term and its contribution to potential leaks through the formation. Indeed, it could trigger a self-feed chain reaction whereby pore fluid could migrate in the new space and fluid pressure would likely further enhance rock fracturing (Beauheim et al. 1993). Although the vast majority of microfractures are surrounded by halite crystals likely to self-heal, no work has reported so far what the outcome would be in the previously described conditions here. Such a study would add important information about damage development in

long-term operations. The impact of second-phase content under mechanical loading conditions linked to gas storage activity still requires more detailed investigations.

7 Conclusions

We investigated the mechanical deformation of five different rock salt samples under cyclic mechanical loading conditions. Our results show that high second-phase content, notably linked to anhydrite layering, acts as a strength weakening agent on both axial and lateral strains accommodating larger brittle deformation in comparison to samples with a lower content in secondary minerals. This rheological behavior is further exacerbated by cycling the mechanical conditions visible from marked changes in the elastic parameters. Halite grains seems to accommodate most of the induced deformation via brittle deformation with microfracturing which is directly linked to the presence of second-phase content such as anhydrite and clay. Two types of porosity enhancement are observed. New porosity is created around isolated crystals of second-phase minerals as a result of grain rotation under cyclic mechanical deformation, without further connectivity nor impact on permeability. Porosity is also generated in areas with high concentration of secondary minerals (such as anhydrite, polyhalite, carnallite, or kieserite) significantly contributing to the microfracture connectivity hence likely increasing permeability. Overall, these porosity changes would have implications for the behavior of the material should the permeability increase by other means. Further investigation is needed to assess the long-term microbrittle deformation linked to second-phase content under cyclic loading conditions.

Open Access This article is licensed under a Creative Commons Attribution 4.0 International License, which permits use, sharing, adaptation, distribution and reproduction in any medium or format, as long as you give appropriate credit to the original author(s) and the source, provide a link to the Creative Commons licence, and indicate if changes were made. The images or other third party material in this article are included in the article's Creative Commons licence, unless indicated otherwise in a credit line to the material. If material is not included in the article's Creative Commons licence and your intended use is not permitted by statutory regulation or exceeds the permitted use, you will need to obtain permission directly from the copyright holder. To view a copy of this licence, visit <http://creativecommons.org/licenses/by/4.0/>.

References

- Av B, Mahmoudi E, Khaledi K, Konig D, Schanz T (2016) Innovative concept for analysing a rock salt cavern under cyclic thermo-mechanical loading. *Energy Procedia* 97(2016):478–485
- Beauheim RL, Wawersik WR, Roberts RM (1993) Coupled permeability and hydrofracture tests to assess the waste-containment properties of fractured anhydrite. In: The 34th US symposium on rock mechanics (USRMS). American Rock Mechanics Association
- Berest P (2011) Aspects of high frequency cycling in salt storage caverns. In: International gas union research conference
- Bérest Pierre et al (2013) Rapid depressurizations: can they lead to irreversible damage?. arXiv preprint [arXiv:1302.2582](https://arxiv.org/abs/1302.2582)
- Berest P, Brouard B, Karimi-Jafari M, (2005) Deep salt caverns abandonment. *Post-Mining*, (2005) November 16–17. Nancy, France
- Berest P, Karimi-Jafari M, Brouard B, Bazargan B (2006) In situ mechanical tests in salt caverns. *Solution Mining Institute*, Spring 2006 Technical Meeting. Brussels, Belgium, May 1–3, 2006
- Beutel T, Black S (2005) Salt deposits and gas cavern storage in the UK with a case study of salt exploration from Cheshire. *Oil Gas Eur Mag* 1:31–35
- Biehl BC, Reuning L, Strozky F, Kukula PA (2014) Origin and deformation of intra-salt sulphate layers: an example from the Dutch Zechstein (Late Permian). *Int J Earth Sci* 103(3):697–712
- British Geological Survey (BGS) (2016) Underground natural gas storage in the UK. Source address: <http://www.bgs.ac.uk/research/energy/undergroundGasStorage.html>
- Brouard B et al (2013) Creep closure rate of a shallow salt cavern at Gellenoncourt, France. *Int J Rock Mech Min Sci* 62:42–50
- Brückner D, Lindert A, Wiedemann M (2003) The Bernburg Test Cavern—a model study of Cavern Abandonment, SMRI Fall Meeting, 5–8. Oct. 2003, Chester, UK, pp 69–89
- Bullough Chris et al (2004) Advanced adiabatic compressed air energy storage for the integration of wind energy. In: *Proceedings of the European wind energy conference, EWEC*, vol. 22
- Carter NL, Hansen FD, Senseny PE (1982) Stress magnitudes in natural rock salt. *J Geophys Res* 87(B11):9289–9300
- Cooper AH (2002) Halite karst geohazards (natural and man-made) in the United Kingdom. *Environ Geol* 42(5):505–512
- Desbois G, Závada P, Schléder Z, Urai JL (2010) Deformation and recrystallization mechanisms in actively extruding salt fountain: microstructural evidence for a switch in deformation mechanisms with increased availability of meteoric water and decreased grain size (Qum Kuh, central Iran). *J Struct Geol* 32:580–594
- Dodds PE, McDowall W (2013) The future of the UK gas network. *Energy Policy* 60:305–316
- Drury MR, Urai JL (1990) Deformation-related recrystallization processes. *Tectonophysics* 172(3–4):235–253
- Evans DJ, Chadwick RA (2009) Underground gas storage: an introduction and UK perspective. In: Evans DJ, Chadwick RA (eds) *Underground Gas Storage: Worldwide Experiences and Future Development in the UK and Europe*. The Geological Society, London, Special Publications, 313, pp 1–11. The Geological Society of London 2009. <https://doi.org/10.1144/SP313.1>
- Evans DJ, Holloway S (2009) A review of onshore UK salt deposits and their potential for underground gas storage. *Geol Soc Lond Spec Publ* 313(1):39–80
- Fan J et al (2017) Discontinuous cyclic loading tests of salt with acoustic emission monitoring. *Int J Fatigue* 9:140–144
- Fan J, Chen J, Jiang D, Ren S, Wu J (2016) Fatigue properties of rock salt subjected to interval cyclic pressure. *Int J Fatigue* 90(2016):109–115
- Fan J, Jiang D, Liu W, Wu F, Chen J, Daemen JJK (2019) Discontinuous fatigue of rock salt with low-stress intervals. *Int J Rock Mech Min Sci* 115:77–86
- Han G et al (2006) Gas storage and operations in single bedded salt caverns: stability analyses. In: *Golden Rocks 2006, The 41st US symposium on rock mechanics (USRMS)*. American Rock Mechanics Association

- Hickman SH, Evans B (1995) Kinetics of pressure solution at halite-silica interfaces and intergranular clay films. *J Geophys Res Solid Earth* 100(B7):13113–13132
- Howard AS, Warrington G, Ambrose K, Rees JG (2008) A formational framework for the Mercia Mudstone Group (Triassic) of England and Wales: Research Report RR/08/04. British Geological Survey International Centre for Diffraction Data (ICDD) PDF-4 2018 – ICDD (2020) JCPDS-International Centre for Diffraction Data. www.icdd.com/pdf-4. Accessed 25 Mar 2020
- International Society for Rock Mechanics (ISRM) (1979) Suggested methods for determining compressive strength and deformability. ISRM, Salzburg
- Jiang D, Fan J, Chen J, Li L, Cui Y (2016) A mechanism of fatigue in salt under discontinuous cycle loading. *Int J Rock Mech Min Sci* 86(2016):255–260
- Khaledi K, Mahmoudi E, Datcheva M, Schanz T (2016) Stability and serviceability of underground energy storage caverns in rock salt subjected to mechanical cyclic loading. *Int J Rock Mech Min Sci* 86(2016):115–131
- Kossow D, Krawczyk CM (2002) Structure and quantification of processes controlling the evolution of the inverted NE-German Basin. *Mar Pet Geol* 19(5):601–618
- Leitner C, Neubauer F, János UL, Schoenherr J (2011) Structure and evolution of a rocksalt-mudrock-tectonite: the Haselgebirge in the Northern Calcareous Alps. *J Struct Geol* 33(5):970–984 (Elsevier)
- Li F et al (2015) Inhomogeneous creep deformation in metallic glasses. *Mater Sci Eng A* 648:57–60
- Li J et al (2019) Modeling the construction of energy storage salt caverns in bedded salt. *Appl Energy* 255:113866
- Li SY, Urai JL (2016) Rheology of rock salt for salt tectonics modeling. *Pet Sci* 13(4):712–724
- Li S, Abe S, Urai JL, Strozyk F, Kukla PA, Van Gent H, Berest P, Ghoreychi M, Hadj-Hassen F, Tijani M (2012) A method to evaluate long-term rheology of Zechstein salt in the Tertiary. In: Proceedings of mechanical behaviour of salt VII. pp 215–220
- Liang W et al (2007) Experimental investigation of mechanical properties of bedded rock salt. *Int J Rock Mech Min Sci* 44(3):400–411
- Liang W et al (2012) Experiments on mechanical properties of rock salts under cyclic loading. *J Rock Mech Geotech Eng* 4(1):54–61
- Liang WG, Zhao YS, Xu SG, Dusseault MB (2011) Effect of strain rate on the mechanical properties of rock salt. *Int J Rock Mech Min Sci* 48:161–167
- Linckens J, Zulauf G, Hammer J (2016) Experimental deformation of coarse-grained rock salt to high strain. *J Geophys Res Solid Earth* 121(8):6150–6171
- Lohkämper TH, Jordan G, Costamagna R, Stöckhert B, Schmahl WW (2003) Phase shift interference microscope study of dissolution-precipitation processes of nonhydrostatically stressed halite crystals in solution. *Contrib Miner Petrol* 146(3):263–274
- Lund H, Salgi G (2009) The role of compressed air energy storage (CAES) in future sustainable energy systems. *Energy Convers Manage* 50(5):1172–1179
- Ma L, Liu X, Wang M, Xu H, Hua R, Fan P, Jiang S, Wang G, Yi Q (2013) Experimental investigation of the mechanical properties of rock salt under triaxial cyclic loading. *Int J Rock Mech Min Sci* 62(2013):34–41
- Martin B, Röller K, Stöckhert B (1999) Low-stress pressure solution experiments on halite single-crystals. *Tectonophysics* 308(3):299–310
- Michalski J, Bünger U, Crotogino F, Donadei S, Schneider GS, Pregar T, Heide D (2017) Hydrogen generation by electrolysis and storage in salt caverns: Potentials, economics and systems aspects with regard to the German energy transition. *Int J Hydrogen Energy* 42(19):13427–13443
- Moghadam SN et al (2015) Parametric assessment of salt cavern performance using a creep model describing dilatancy and failure. *Int J Rock Mech Min Sci* 79:250–267
- Moghadam NS, Mirzabozorg H, Noorzad A (2013) Modeling time-dependent behavior of gas caverns in rock salt considering creep, dilatancy and failure. *Tunn Undergr Space Technol* 33:171–185
- Norton GE, Bloodworth AJ, Cameron DG, Evans DJ, Lott GK, Hobbs SF, Spencer NA, Highley DE (2005) Mineral resource information in support of national, regional and local planning—Cheshire (comprising Cheshire, Boroughs of Halton and Warrington). Commissioned Report, CR/05/090N
- Othmar S (1986) Bau und Bildung der Salzlagerstätten des ostalpinen Salinars. *Archiv für Lagerstättenforschung der Geologischen Bundesanstalt*. 7:217–254
- Ozarslan A (2012) Large-scale hydrogen energy storage in salt caverns. *Int J Hydrogen Energy* 37:14265–14277
- Parliament HM (2008) The Climate Change Act 2008. London UK
- Peach CJ (1991) Influence of deformation on the fluid transport properties of rock salts. *Geol Ultraiect* 77:1–238
- Pfiffle TW, Senseny PE (1981) Elastic-plastic deformation of anhydrite and polyhalite as determined from quasi-static triaxial compression tests. No. SAND–81-7063. RE/SPEC
- Pierre B et al (eds) (2012) Mechanical behaviour of salt VII. CRC Press, New York
- Pluymakers AMH, Niemeijer AR (2015) Healing and sliding stability of simulated anhydrite fault gouge: effects of water, temperature and CO₂. *Tectonophysics* 656:111–130
- Renard F, Bernard D, Thibault X, Boller E et al (2004) Synchrotron 3D microtomography of halite aggregates during experimental pressure solution creep and evolution of the permeability. *Geophys Res Lett* 31:L07607
- Renard F, Dysthe D, Feder J, Jamtveit B (2002) Healing of fluid-filled microcracks. In: Proceedings of the second Biot conference on poromechanics. pp 925–31
- Sadler D et al (2016) H21 leeds city gate. Leeds City Gate, Northern Gas Networks, Wales and West Utilities, p 1325
- Schenk O, Urai JL (2004) Microstructural evolution and grain boundary structure during static recrystallization in synthetic polycrystals of sodium chloride containing saturated brine. *Contrib Mineral Petrol* 146(6):671–682 (Springer)
- Schenk O, Urai JL, Piazzolo S (2006) Structure of grain boundaries in wet, synthetic polycrystalline, statically recrystallizing halite-evidence from cryo-SEM observations. *Geofluids* 6(1):93–104
- Schleéder Z, Urai JL (2005) Microstructural evolution of deformation-modified primary halite from Hengelo. The Netherlands. *Int J Earth Sci* 94(5–6):941–56
- Schulze O, Popp T, Kern H (2001) Development of damage and permeability in deforming rock salt. *Eng Geol* 61(2–3):163–180
- Senseny et al (1992) Mechanical behaviour of rock salt: phenomenology and micromechanisms. *Int J Rock Mech Min Sci Geomech Abstr* 29(4):363–378
- Serbin K, Slizowski J, Urbanczyk K, Nagy S (2015) The influence of thermodynamic effects on gas storage cavern convergence. *Int J Rock Mech Min Sci* 79(2015):166–171
- Spiers CJ, Brzesowsky RH (1993) Densification behaviour of wet granular salt: theory versus experiment. In: Kakihana H, Hardy HR, Hoshi T Jr, Toyokura K (eds) Seventh symposium on salt. Elsevier, Amsterdam, pp 83–92
- Spiers CJ, Schutjens PMTM (1999) Intergranular pressure solution in NaCl: grain-to-grain contact experiments under the optical microscope. *Oil Gas Sci Technol* 54(6):729–750
- Spiers CJ, Schutjens PMTM, Brzesowsky RH, Peach CJ, Liezenberg JL, Zwart HJ (1990) Experimental determination of constitutive parameters governing creep of rocksalt by pressure solution. In: Knipe RJ, Rutter EH (eds) Deformation mechanisms, rheology

- and tectonics, vol 54, 1st edn. Geological Society, London, pp 215–27 (**Special Publications**)
- Strohmeier C, Strauss C (1996) Sedimentology and palynofacies of the Zechstein 2 Carbonate (Upper Permian, Northwest Germany): implications for sequence stratigraphic subdivision. *Sed Geol* 102(1–2):55–77
- Urai JL et al (2008) Flow and transport properties of rock salts. The central European basin system. Dynamics of complex intracontinental basins, pp 277–290
- Urai JL, Spiers CJ (2007) The effect of grain boundary water on deformation mechanisms and rheology of rock salt during long-term deformation. In: Proceedings of 6th conference on the mechanical behavior of salt
- Urai JL (1983) Water assisted dynamic recrystallization and weakening in polycrystalline bischofite. *Tectonophysics* 96(1–2):125–157
- Urai JL, Means WD, Lister GS (1986) Dynamic recrystallization of minerals. *Mineral and rock deformation: laboratory studies*, vol 36. AGU, Washington, DC, pp 161–199
- Van Sambeek LL, Ratigan JL, Hansen FD (1993) Dilatancy of rock salt in laboratory tests. *Int J Rock Mech Min Sci Geomech Abstr* 30(7):735–738
- Van Wees J-D et al (2000) On the origin of the southern Permian Basin. Central Europe. *Mar Pet Geol* 17(1):43–59
- Voznesenskii AS, Krasilov MN, Kutkin YO, Tavostin MN, Osipov YV (2017) Features of interrelations between acoustic quality factor and strength of rock salt during fatigue cyclic loadings. *Int J Fatigue* 97:70–78
- Wang T et al (2013) A new shape design method of salt cavern used as underground gas storage. *Appl Energy* 104:50–61
- Wang T et al (2016) Safety evaluation of salt cavern gas storage close to an old cavern. *Int J Rock Mech Min Sci* 83:95–106
- Wawersik WR, Preece DS (1982) Creep testing of salt: procedures, problems and suggestions. No. SAND-81-1116C. Sandia National Labs
- Xiong J, Huang X, Ma H (2015) Gas leakage mechanism in bedded rock salt storage cavern considering damaged interface. *Petroleum* 1(2015):366–372
- Závada P et al (2015) Impact of solid second phases on deformation mechanisms of naturally deformed rock salts (Kuh-e-Namak, Dashti, Iran) and rheological stratification of the Hormuz Salt Formation. *J Struct Geol* 74:117–144
- Zhang Y, Krause M, Mutti M (2013) The formation and structure evolution of Zechstein (Upper Permian) Salt in Northeast German Basin: a review. *Open J Geol* 3:411–426
- Zhao B, Huang T, Dongyan L, Liu D, Liu Y, Wang X (2020) Experimental study and damage model study of rock salt subjected to cyclic loading and cyclic creep. *Adv Civ Eng* 2020
- Zhenyu TAO, Haihong MO (1990) An experimental study and analysis of the behaviour of rock under cyclic loading. *Int J Rock Mech Min Sci Geomech Abstr* 27:1
- Ziegler PA (1990) Geological atlas of western and central Europe. Geological Society of London, 239 pp

Publisher's Note Springer Nature remains neutral with regard to jurisdictional claims in published maps and institutional affiliations.